EVOLUTION, NUCLEOSYNTHESIS, AND YIELDS OF AGB STARS AT DIFFERENT METALLICITIES. III. INTERMEDIATE-MASS MODELS, REVISED LOW-MASS MODELS, AND THE pH-FRUITY INTERFACE

S. Cristallo[1,2], O. Straniero[1,3], L. Piersanti[1,2], and D. Gobrecht[1]
[1] INAF-Osservatorio Astronomico di Collurania, I-64100 Teramo, Italy
[2] INFN Sezione Napoli, Napoli, Italy
[3] INFN LNGS, Assergi, Italy

ABSTRACT

We present a new set of models for intermediate-mass asymptotic giant branch (AGB) stars (4.0, 5.0, and 6.0 $M_\odot$) at different metallicities ($-2.15 \leqslant [\mathrm{Fe/H}] \leqslant +0.15$). This set integrates the existing models for low-mass AGB stars ($1.3 \leqslant M/M_\odot \leqslant 3.0$) already included in the FRUITY database. We describe the physical and chemical evolution of the computed models from the main sequence up to the end of the AGB phase. Due to less efficient third dredge up episodes, models with large core masses show modest surface enhancements. This effect is due to the fact that the interpulse phases are short and, therefore, thermal pulses (TPs) are weak. Moreover, the high temperature at the base of the convective envelope prevents it from deeply penetrating the underlying radiative layers. Depending on the initial stellar mass, the heavy element nucleosynthesis is dominated by different neutron sources. In particular, the s-process distributions of the more massive models are dominated by the $^{22}\mathrm{Ne}(\alpha,\mathrm{n})^{25}\mathrm{Mg}$ reaction, which is efficiently activated during TPs. At low metallicities, our models undergo hot bottom burning and hot third dredge up. We compare our theoretical final core masses to available white dwarf observations. Moreover, we quantify the influence intermediate-mass models have on the carbon star luminosity function. Finally, we present the upgrade of the FRUITY web interface, which now also includes the physical quantities of the TP-AGB phase for all of the models included in the database (ph-FRUITY).

Key words: nuclear reactions, nucleosynthesis, abundances – Stars: AGB and post-AGB

1. INTRODUCTION

Asymptotic giant branch (AGB) stars are ideal laboratories to test our understanding of stellar interiors. The evolution of such objects is characterized by a sequence of burning and mixing episodes which carry the nuclear products synthesized in the internal layers to the stellar surface. During the AGB, the structure consists of a partially degenerate CO core, an He-shell, and an H-shell separated by a thin helium-rich layer (the so-called He-intershell) and an expanded and cool convective envelope. The surface luminosity is mainly sustained by the H-burning shell. This situation is repeatedly interrupted by the growth of thermonuclear runaway thermal pulses (TPs) in the He-intershell, triggered by the activation of 3α reactions. The rate of nuclear energy is too large to be carried away by radiation, and thus a convective shell develops which makes the He-intershell chemically homogenous. Then, the layers above expand and cool until the convective shell is quenched. If the expansion has been large enough, then the H-shell switches off and the convective envelope can penetrate the H-exhausted and chemically enriched He-intershell (this phenomenon is known as Third Dredge Up, TDU). Meanwhile, the products of internal nucleosynthesis appear on the stellar surface. During AGB, a strong stellar wind erodes the convective envelope, thus polluting the interstellar medium. AGB stars efficiently synthesize both light (C, N, F, and Na) and heavy elements (those created via the slow neutron capture process, the s-process). The interested reader can find a vast body of literature on AGB stars (Iben & Renzini 1983; Herwig 2005; Straniero et al. 2006; Karakas & Lattanzio 2014).

Sets of AGB stars need uniform (i.e., computed with the same code) and complete (i.e., containing a large number of masses) information in order to properly describe the chemical

evolution of the host systems. For the past several years, we have made our AGB yields available on the FRUITY database (Cristallo et al. 2009, 2011). Through a web interface, we provide tables of the isotopic and elemental compositions as well as the stellar yields of AGB stars. To date, FRUITY only includes low-mass stars (i.e., stars with initial masses $M \leqslant 3$ $M_\odot$). In this paper, we present a new set of AGB models with larger initial masses ($4 \leqslant M/M_\odot \leqslant 6$). The evolution of those objects resembles that of their low-mass counterparts, even if noticeable differences exist. In particular, their larger initial masses produce more compact cores, and thus larger temperatures can be obtained in their interiors. Consequently, the physical conditions for triggering He burning in the He intershell are reached earlier during the AGB phase compared to models with lower initial masses. Thus, the interpulse phases are shorter, the TPs are weaker, and the efficiency of TDU is strongly reduced (Straniero et al. 2003a). Moreover, the larger the initial stellar mass, the larger the mass extension of the convective envelope (this fact implies a larger dilution of the dredged-up material). Consequently, we obtain modest surface chemical enrichments in the more massive AGBs. Furthermore, in those objects, processes such as hot bottom burning (HBB; Sugimoto 1971; Iben 1973) and hot-TDU (H-TDU; Goriely & Siess 2004; Straniero et al. 2014) can be active. During HBB, temperatures become high enough to partially activate the CN cycle at the base of the convective envelope. Thus, considerable amounts of $^{13}\mathrm{C}$ and $^{14}\mathrm{N}$ can be produced. The main effect of H-TDU, on the other hand, is to limit the penetration of the convective envelope itself because the temperature for the reactivation of the H-shell is soon attained. Thus, H-TDU further weakens the TDU efficiency.

In AGB stars, two major neutron sources are at work: the $^{13}\mathrm{C}$ $(\alpha,\mathrm{n})^{16}\mathrm{O}$ and $^{22}\mathrm{Ne}(\alpha,\mathrm{n})^{25}\mathrm{Mg}$ reactions. In low-mass stars, the

Table 1
Initial Helium and α Enrichment for Different Initial Masses and Metallicities (bold labels refer to models added with this work)

Mass/Z	2.4×10^{-4}	7.2×10^{-4}	1.0×10^{-3}	2.0×10^{-3}	3.0×10^{-3}	6.0×10^{-3}	8.0×10^{-3}	1.0×10^{-2}	1.4×10^{-2}	2.0×10^{-2}
Mass/[Fe/H]	-2.15	-1.67	-1.15	-0.85	-0.67	-0.37	-0.24	-0.15	0.00	0.15
1.3	(0.245;0.5)	(0.245;0.5)	(0.245;0)	**(0.252;0)**	(0.260;0)	(0.260;0)	(0.265;0)	(0.265;0)	(0.269;0)	(0.269;0)
1.5	(0.245;0.5)	(0.245;0.5)	(0.245;0)	**(0.252;0)**	(0.260;0)	(0.260;0)	(0.265;0)	(0.265;0)	(0.269;0)	(0.269;0)
2.0	(0.245;0.5)	(0.245;0.5)	(0.245;0)	**(0.252;0)**	(0.260;0)	(0.260;0)	(0.265;0)	(0.265;0)	(0.269;0)	(0.269;0)
2.5	(0.245;0.5)	(0.245;0.5)	(0.245;0)	**(0.252;0)**	(0.260;0)	(0.260;0)	(0.265;0)	(0.265;0)	(0.269;0)	(0.269;0)
3.0	(0.245;0.5)	(0.245;0.5)	(0.245;0)	**(0.252;0)**	(0.260;0)	(0.260;0)	(0.265;0)	(0.265;0)	(0.269;0)	(0.269;0)
4.0	**(0.245;0.5)**	(0.245;0.5)	**(0.245;0)**	**(0.252;0)**	**(0.260;0)**	**(0.260;0)**	**(0.265;0)**	**(0.265;0)**	**(0.269;0)**	**(0.269;0)**
5.0	**(0.245;0.5)**	(0.245;0.5)	**(0.245;0)**	**(0.252;0)**	**(0.260;0)**	**(0.260;0)**	**(0.265;0)**	**(0.265;0)**	**(0.269;0)**	**(0.269;0)**
6.0	**(0.245;0.5)**	(0.245;0.5)	**(0.245;0)**	**(0.252;0)**	**(0.260;0)**	**(0.260;0)**	**(0.265;0)**	**(0.265;0)**	**(0.269;0)**	**(0.269;0)**

dominant contribution to s-process nucleosynthesis comes from the ^{13}C$(\alpha,n)^{16}$O reaction. The ^{13}C reservoir, i.e., the so-called ^{13}C pocket, forms during TDU episodes in the top layers of the H-exhausted He intershell (for details see Cristallo et al. 2011). In more massive AGBs, due to the limitations of the H-TDU, the contribution from the ^{13}C reaction is definitely lower, while an important contribution comes from[4] ^{22}Ne$(\alpha,n)^{25}$Mg . In fact, in such objects, this reaction is efficiently activated at the base of the convective shells generated by TPs. This neutron source significantly contributes to the production of rubidium and light s-process elements. Thus, s-process surface distributions with different shapes and enhancements can be found by varying the metallicity and the initial stellar mass. In fact, the three s-process peaks[5] receive different contributions depending on the physical environmental conditions (radiative or convective burning) and on the neutron-to-seed ratio (which is related to the metallicity).

In this paper, we also illustrate a new web interface (ph-FRUITY) for accessing tables containing the evolution of the most relevant physical quantities of our models.

This paper is structured as follows. In Section 2, we describe the main features of our stellar evolutionary code, focusing on the most recent upgrades. In Section 3, we highlight the evolutionary phases prior to the AGB, which is analyzed in Section 4. In Section 5, we show the potential of our new web ph-FRUITY interface. The nucleosynthesis of all of the FRUITY models is discussed in detail in Section 6. Finally, in Section 7 we report the discussion and our conclusions.

2. THE MODELS

As has already been outlined, the models presented in this paper (4.0-5.0-6.0 $M_\odot$) integrate the pre-existing set available on the FRUITY database (Cristallo et al. 2011), currently hosting low-mass star AGB (hereafter LMS-AGB; 1.3-1.5-2.0-2.5-3.0) models with different initial metallicities ($-2.15 \leqslant$ [Fe/H] $\leqslant +0.15$). We add an additional metallicity ($Z = 0.002$, corresponding to [Fe/H] $= -0.85$) in order to better sample the peak in lead production (see below). In Table 1, we report all of the models included in the FRUITY database (we show in bold those models added by this work), specifying the initial He content, the [Fe/H], and the eventual α enrichment. In the table header, we report both [Fe/H] and the corresponding total metallicity (which takes into account

the eventual α enhancement). The isotopic initial distribution of each model is assumed to be solar-scaled (apart from the eventual α-enhanced isotopes, i.e., ^{16}O, ^{20}Ne, ^{24}Mg, ^{28}Si, ^{32}S, ^{36}Ar, and ^{40}Ca). We adopt the solar distribution presented by Lodders (2003). The models have been computed with the FUNS evolutionary code (Straniero et al. 2006; Cristallo et al. 2009). The physical evolution of the star is coupled to a nuclear network including all isotopes (from hydrogen to lead, at the termination of the s-process path). Thus, we do not need to perform any post-processing calculations to determine the nucleosynthetic yields. The list of reactions and the adopted rates are the same as in Cristallo et al. (2011). Among the various physical processes, convection and mass loss mainly affect the AGB evolution (and thus the correlated stellar yields and surface distributions). We determine the convective velocities following the prescriptions of the mixing length theory (MLT; Böhm-Vitense 1958), according to the derivation of Cox (1968). In the framework of MLT, corresponding to a convective border, the velocity is zero if the adiabatic temperature gradient presents a smooth profile.[6] However, during a TDU episode, there is a sharp discontinuity in the opacity profile (and thus in the radiative gradient). This makes the convective/radiative interface unstable. In order to handle such a situation, we apply an exponentially decreasing profile of convective velocities below the formal Schwarzschild border (Straniero et al. 2006). This implies a more efficient TDU and, as a by-product, the formation of a tiny ^{13}C pocket. In fact, such non-convective mixing allows some protons to penetrate the formal border of the convective envelope. Those protons are captured by the abundant ^{12}C (the product of 3α processes) leading to the formation of a region enriched in ^{13}C (commonly known as the ^{13}C pocket). In Cristallo et al. (2009), we demonstrated that the extension in mass of the ^{13}C pocket decreases along the AGB (thus with increasing core masses), following the shrinking and compression of the He-intershell region. Therefore, we expect that the contribution to s-process nucleosynthesis from the ^{13}C pocket is strongly reduced in massive AGBs with respect to their low-mass counterparts (see Section 4). In the following, we define intermediate-mass stars (IMS) as those approaching the TP-AGB phase with a mass of the H-exhausted core greater than 0.8 $M_\odot$ (see Section 3).

Another very uncertain physical input for AGB models is the mass-loss rate, which largely determines, for instance, the duration of the AGB and the amount of H-depleted dredged-up material after each TDU. During the AGB, large-amplitude

---

[4] Abundant ^{22}Ne is the final product of the ^{14}N$(\alpha,\gamma)^{18}$F$(\beta^+)^{18}$O$(\alpha,\gamma)^{22}$Ne nuclear chain.

[5] The three s-process components are ls (Sr–Y–Zr), hs (Ba–La–Nd–Sm), and lead (Pb).

[6] We note that the velocity is proportional to the difference between the radiative and adiabatic temperature gradients.

pulsations induce the formation of shocks in the most external stellar layers. As a result, the local temperature and density increase and a rich and complex chemistry develops, leading to the creation of molecules and dust grains. Those small particles interact with the radiation flux and drive strong stellar winds. Available observational data indicate that in galactic AGB stars, the mass-loss ranges between 10^{-8} and 10^{-4} $M_\odot \, \mathrm{yr}^{-1}$ with a clear correlation with the pulsational period (Vassiliadis & Wood 1993), at least for long periods (see Uttenthaler 2013). Since the pulsational period depends on variations in radius, luminosity, and mass, a relation between the mass-loss rate and the basic stellar parameters can be derived. By adopting a procedure similar to that in Vassiliadis & Wood (1993), we revised the mass-loss-period relation taking into account more recent infrared observations of AGB stars (see Straniero et al. 2006 and references therein) and based on the observed correlation between periods and luminosities in the K band (see, e.g., Whitelock et al. 2003). The few pulsation masses derived to date for AGB stars (Wood 2007) do not allow the identification of trends in the mass-loss-period relation as a function of the stellar mass.[7] Thus, we apply the same theoretical recipe for the whole mass range in our models, even if other mass-loss prescriptions are available for luminous oxygen-rich AGB giants. For instance, we could use the mass-loss rate proposed by van Loon et al. (2005). However, when applying that formula to our low-metallicity models, the mass loss practically vanishes, and therefore we exclude it.

When dealing with C-rich objects, particular attention should be paid to the opacity treatment of the most external (and cool) regions. As has already been discussed, molecules efficiently form in those layers. Depending on the C/O ratio, O-bearing or C-bearing molecules form, leading to dichotomic behaviors in the opacity regime. C-bearing molecules, in fact, are more opaque, and thus increase the opacity of the layer where they form. Consequently, the radiation struggles to escape from the stellar structure and, therefore, the most external layers expand and cool. This naturally implies an enhancement in the mass-loss rate, which strongly depends on the stellar surface temperature. It has been demonstrated that the use of low-temperature C-bearing opacities has dramatic consequences for the physical evolution of AGB stars (Marigo 2002; see also Cristallo et al. 2007 and Ventura & Marigo 2010). For solar-scaled metallicities, we adopt the opacities from Lederer & Aringer (2009), while for α-enhanced mixtures we use the AESOPUS tool (Marigo & Aringer 2009), which allows us to freely vary the chemical composition. In calculating the IMS-AGB models, we found an erroneous treatment of opacities in the most external layers of the stars, enclosing about 2% of the total mass. Then, we verified one by one all of the low-mass models already included in the FRUITY database; for some of them, we found significant variations in the final surface composition. We discuss this problem in Section 6.

3. FROM THE PRE-MAIN SEQUENCE (MS) TO THE TP-AGB PHASE

We follow the evolution of the models listed in Table 1 from the pre-MS up to the AGB tip. The computations terminate when the H-rich envelope is reduced below the threshold for
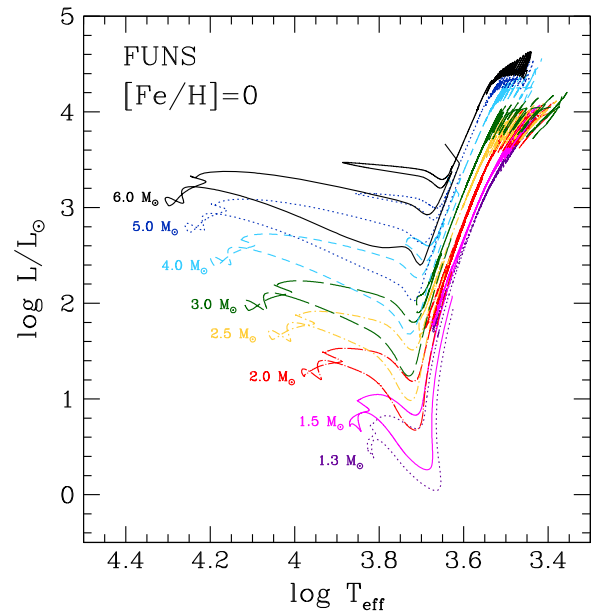
Figure 1. Hertzsprung–Russell diagram for models with initial solar metallicity.

TDU occurrence. The Hertzsprung–Russell tracks of the solar metallicity set are shown in Figure 1.

In this section, we briefly revise the evolution until the beginning of the TP-AGB phase. For a more detailed description of these phases, see Dominguez et al. (1999). All of the evolutionary sequences start from a homogeneous and relatively cool model relaxed on the Hayashi track, i.e., the first fully convective models in hydrostatic and thermal equilibrium. As usual, stars enter the MS when all of the secondary isotopes involved in the p–p chain and the CNO cycle attain equilibrium in the central region. Table 2 reports the MS lifetimes for the whole data set.[8] In Equation (1), we provide a simple interpolation formula linking the MS lifetime to the initial mass and metallicity of the model:

$$\tau_{\mathrm{MS}} = 9.775 + 9.898 {}^{*}Z - 1.460 {}^{*} ln(M) + 0.152 {}^{*} (ln(M))^2.$$

(1)

The variations of these lifetimes reflect the well-known non-linearity of the mass–luminosity relation for MS stars. The less massive models (1.3 $M_\odot$) mark the transition between the lower MS (consisting of stars whose luminosity is mainly controlled by the p–p nuclear chain and characterized by a radiative core and a convective envelope) and the upper MS (whose stars burn H through the CNO cycle and develop a convective core, while their envelope remains fully radiative). The convective core attains a maximum extension just after the beginning of the MS. Then, its extension decreases as H is converted into He and, consequently, the radiative opacity decreases. The maximum extension of the convective core is reported in Table 3. No convective core overshoot has been assumed in these models. Central convection eventually disappears when the central H mass fraction drops below ∼0.1. Then, an overall contraction occurs. The tip of the MS, i.e., the relative

---

[7] Note that Vassiliadis & Wood (1993) delayed the onset of the super-wind phase in stars with masses greater than 2.5 $M_\odot$.

[8] For completeness, we also include data previously reported in Cristallo et al. (2011).

Table 2
Main-sequence Lifetimes (yr) for Different Initial Masses and Metallicities

| Mass/[Fe/H]	−2.15	−1.67	−1.15	−0.85	−0.67	−0.37	−0.24	−0.15	0.00	0.15
1.3	2.38E+09	2.38E+09	2.45E+09	2.50E+09	2.53E+09	2.95E+09	3.15E+09	3.49E+09	3.75E+09	4.76E+09
1.5	1.51E+09	1.51E+09	1.56E+09	1.60E+09	1.61E+09	1.85E+09	1.98E+09	2.16E+09	2.31E+09	2.84E+09
2.0	6.25E+08	6.51E+08	6.80E+08	7.12E+08	7.12E+08	8.10E+08	8.44E+08	9.13E+08	9.70E+08	1.16E+09
2.5	3.44E+08	3.60E+08	3.75E+08	3.88E+08	3.82E+08	4.30E+08	4.47E+08	4.79E+08	5.03E+08	5.92E+08
3.0	2.20E+08	2.28E+08	2.35E+08	2.42E+08	2.38E+08	2.64E+08	2.71E+08	2.88E+08	2.99E+08	3.46E+08
4.0	1.14E+08	1.16E+08	1.20E+08	1.20E+08	1.19E+08	1.29E+08	1.32E+08	1.39E+08	1.44E+08	1.66E+08
5.0	7.11E+07	7.17E+07	7.30E+07	7.23E+07	7.11E+07	7.53E+07	7.65E+07	7.97E+07	8.19E+07	9.10E+07
6.0	4.95E+07	4.95E+07	4.98E+07	4.91E+07	4.80E+07	5.03E+07	5.07E+07	5.24E+07	5.34E+07	5.80E+07

Table 3
Maximum Size of the Convective Core Developed during the MS (in Solar Units)

Mass/[Fe/H]	−2.15	−1.67	−1.15	−0.85	−0.67	−0.37	−0.24	−0.15	0.00	0.15
1.3	0.147	0.130	0.130	0.111	0.120	0.155	0.164	0.155	0.164	0.155
1.5	0.211	0.200	0.189	0.169	0.169	0.147	0.141	0.136	0.131	0.122
2.0	0.386	0.376	0.365	0.346	0.336	0.327	0.310	0.301	0.293	0.270
2.5	0.569	0.553	0.538	0.524	0.509	0.496	0.483	0.496	0.469	0.444
3.0	0.783	0.761	0.741	0.721	0.702	0.664	0.663	0.646	0.628	0.594
4.0	1.198	1.198	1.133	1.074	1.045	1.015	0.987	0.962	0.962	0.988
5.0	1.606	1.606	1.538	1.457	1.417	1.342	1.342	1.342	1.269	1.342
6.0	2.043	2.043	1.928	1.846	1.797	1.700	1.700	1.700	1.610	1.700

Table 4
The H-exhausted Core Mass at the Beginning of He Burning (in Solar Units)

Mass/[Fe/H]	−2.15	−1.67	−1.15	−0.85	−0.67	−0.37	−0.24	−0.15	0.00	0.15
1.3	0.485	0.487	0.488	0.487	0.485	0.485	0.490	0.490	0.481	0.480
1.5	0.473	0.482	0.484	0.484	0.484	0.484	0.483	0.483	0.481	0.480
2.0	0.404	0.437	0.452	0.451	0.451	0.462	0.463	0.466	0.465	0.471
2.5	0.347	0.344	0.343	0.341	0.324	0.317	0.319	0.317	0.315	0.314
3.0	0.405	0.400	0.397	0.393	0.383	0.383	0.382	0.378	0.375	0.369
4.0	0.533	0.533	0.525	0.518	0.518	0.506	0.504	0.498	0.494	0.484
5.0	0.675	0.666	0.675	0.656	0.656	0.639	0.635	0.630	0.626	0.618
6.0	0.822	0.822	0.822	0.799	0.799	0.782	0.777	0.766	0.766	0.756

maximum in the luminosity, is attained when the central H goes to ∼0. Then, before He ignition, all of the models, except the more massive ones with $Z \leqslant 10^{-3}$, experience a deep mixing episode, i.e., the so-called first dredge up (FDU). The following development of He burning depends on the equation of state of the He-rich core. The values of the He-core masses at ignition well represent this occurrence, as reported in Table 4. For the more massive models ($M \geqslant 3\ M_\odot$), they are essentially determined by the extension of the convective core during the MS. After core-H burning, these stars rapidly proceed toward a quiescent He ignition which occurs at relatively low density. On the contrary, for less massive stars, the core mass slowly grows during the RGB because of shell H burning. For this reason, in stars with $M < 2\ M_\odot$, the central density grows to 10^5–10^6 g cm^{-3} so that the pressure is mainly controlled by degenerate electrons. Under these conditions, He ignition proceeds through thermonuclear runaway (He flash) when the core mass exceeds a critical value of about $0.5\ M_\odot$. In slightly more massive objects ($2 < M/M_\odot < 3$), the electron degeneracy is weaker and the critical core mass for the He ignition is reduced to ∼0.3 $M_\odot$ (see Prada Moroni & Straniero 2009). This behavior is also illustrated in Figure 2; the minimum core mass at He ignition is found for stellar masses $2.0 < M/M_\odot < 2.5$
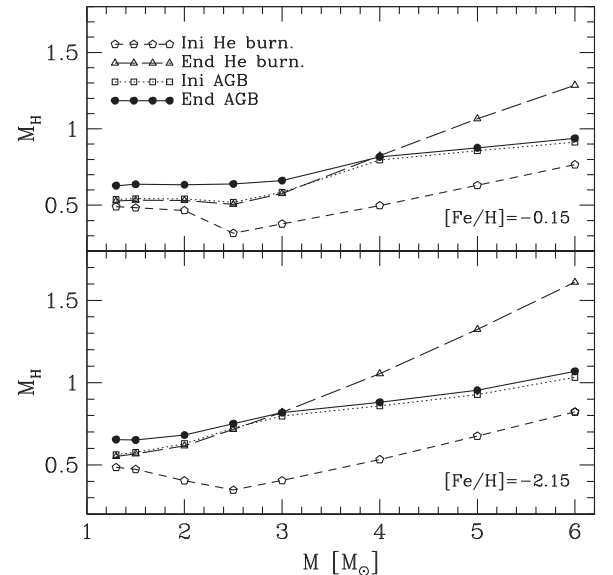
Figure 2. He-exhausted core masses at the beginning of central He burning (pentagons), at the end of central He burning (triangles), at the beginning of AGB (squares), and at the end of AGB (circles).

Table 5
Central Helium Burning Lifetimes (yr) for Different Initial Masses and Metallicities

Mass/[Fe/H]	−2.15	−1.67	−1.15	−0.85	−0.67	−0.37	−0.24	−0.15	0.00	0.15
1.3	8.72E+07	8.95E+07	9.06E+07	9.39E+07	9.64E+07	1.01E+08	9.16E+07	9.23E+07	1.10E+08	1.17E+08
1.5	9.16E+07	9.02E+07	9.08E+07	9.35E+07	9.57E+07	1.00E+06	1.03E+08	1.05E+08	1.09E+08	1.16E+08
2.0	1.13E+08	1.04E+08	1.02E+08	1.11E+08	1.14E+08	1.14E+08	1.16E+08	1.17E+08	1.19E+08	1.22E+08
2.5	9.68E+07	1.11E+08	1.23E+08	1.36E+08	1.51E+08	1.99E+08	2.18E+08	2.42E+08	2.59E+08	3.02E+08
3.0	5.87E+07	6.45E+07	7.05E+07	7.70E+07	7.96E+07	9.75E+07	1.10E+08	1.25E+08	1.38E+08	1.68E+08
4.0	2.67E+07	2.81E+07	3.02E+07	3.28E+07	3.41E+07	3.79E+07	3.92E+07	4.21E+07	4.54E+07	5.68E+07
5.0	1.50E+07	1.56E+07	1.66E+07	1.80E+07	1.87E+07	2.06E+07	2.09E+07	2.19E+07	2.21E+07	2.47E+07
6.0	9.55E+06	9.94E+06	1.04E+07	1.12E+07	1.16E+07	1.28E+07	1.29E+07	1.31E+07	1.34E+07	1.44E+07

Table 6
The H-exhausted Core Mass at the End of He Burning (in Solar Units)

Mass/[Fe/H]	−2.15	−1.67	−1.15	−0.85	−0.67	−0.37	−0.24	−0.15	0.00	0.15
1.3	0.551	0.548	0.544	0.540	0.538	0.533	0.531	0.528	0.527	0.523
1.5	0.567	0.561	0.553	0.547	0.545	0.537	0.535	0.532	0.531	0.525
2.0	0.616	0.604	0.588	0.556	0.550	0.539	0.534	0.531	0.531	0.527
2.5	0.716	0.684	0.660	0.621	0.595	0.531	0.517	0.506	0.506	0.489
3.0	0.819	0.797	0.775	0.736	0.717	0.642	0.607	0.577	0.562	0.536
4.0	1.055	1.045	1.026	0.991	0.968	0.888	0.862	0.824	0.793	0.715
5.0	1.324	1.319	1.300	1.269	1.247	1.133	1.075	1.066	1.052	0.976
6.0	1.610	1.600	1.578	1.556	1.534	1.423	1.355	1.286	1.325	1.245

Table 7
The Total Stellar Mass at the Beginning of the AGB Phase (in Solar Units)

Mass/[Fe/H]	−2.15	−1.67	−1.15	−0.85	−0.67	−0.37	−0.24	−0.15	0.00	0.15
1.3	1.203	1.187	1.177	1.165	1.157	1.134	1.124	1.117	1.109	1.091
1.5	1.422	1.405	1.398	1.388	1.379	1.362	1.354	1.350	1.343	1.330
2.0	1.956	1.942	1.938	1.941	1.938	1.928	1.921	1.915	1.917	1.899
2.5	2.458	2.456	2.457	2.461	2.466	2.477	2.478	2.479	2.475	2.473
3.0	2.957	2.949	2.948	2.950	2.949	2.963	2.969	2.976	2.978	2.981
4.0	3.963	3.943	3.920	3.894	3.837	3.785	3.768	3.807	3.822	3.940
5.0	4.952	4.909	4.862	4.800	4.713	4.578	4.599	4.556	4.516	4.517
6.0	5.886	5.797	5.772	5.645	5.467	5.203	5.203	5.266	5.103	4.970

(see also Sweigart et al. 1990; Dominguez et al. 1999). Table 5 reports the core-He-burning lifetimes. The variation of this quantity reflects the variations of the core mass at He ignition. In fact, the lower the core mass, the fainter the He-burning phase and, in turn, the longer the lifetime. As a result, the longest core-He-burning lifetimes are attained for stellar masses between 2 and 2.5 $M_\odot$. Our core-He-burning models include specific treatments of the instability occurring at the external border of the convective core and semi-convection, as described in Straniero et al. (2003b). During this phase, the core mass further increases due to the shell H burning (see Figure 2). For high metallicities, at the end of the core-He-burning phase, the core mass is nearly constant for M < 3 $M_\odot$ and rapidly increases for larger stellar masses. This limit is smaller at lower Z. The masses of the H-exhausted core at the end of the central He-burning phase are reported in Table 6.

During the early-AGB phase, an He-burning shell forms and advances in mass at a rate that is much higher than that of the pre-existing H-burning shell. In the more massive models, H burning dies down and another mixing episode occurs (the Second Dredge Up, SDU) due to the expansion powered by the He burning and the consequent cooling of the envelope. The lowest stellar mass undergoing an SDU is 3 $M_\odot$ at Z = 0.0001

and 4 $M_\odot$ at Z = 0.02. Table 7 lists the core mass at the onset of the first TP. It practically coincides with the value attained at the end of core-He burning, except for stars undergoing SDU, as clearly shown in Figure 2. Due to the mass lost in the previous evolutionary phases, stars attain the AGB with masses lower than the initial masses. In our models, we adopt a Reimers' parameterization of the mass-loss rate (with $\eta = 0.4$) up to the first TP. In general, only stars with M ⩽ 2 $M_\odot$ (those developing a degenerate He-rich core during the RGB) lose a non-negligible fraction of their initial mass (see Table 8).

The modifications of the chemical compositions induced by FDU and (eventually) SDU are reported in Tables 9 and 10 for two different metallicities ($Z = 1 \times 10^{-2}$ and $Z = 2.4 \times 10^{-4}$, respectively). As expected, after a dredge up episode (FDU or SDU), the models show an increase in the surface helium abundance as well as modified CNO isotopic ratios. It should be noted that the abundances observed at the surface of low-mass ($M < 2.0\ M_\odot$) giant stars at the tip of the RGB often differ from those at FDU due to the presence of a non-convective mixing episode, which links the surface to the hot layers above the H-burning shell. This occurs when stars populate the so-called bump of the luminosity function (see Palmerini et al. 2011 for a discussion on the various proposed physical mechanisms triggering such a mixing; see also Nucci & Busso 2014). Those chemical anomalies have been observed,

Table 8
The H-exhausted Core Mass at the Beginning of the AGB Phase (in Solar Units)

Mass/[Fe/H]	−2.15	−1.67	−1.15	−0.85	−0.67	−0.37	−0.24	−0.15	0.00	0.15
1.3	0.563	0.559	0.554	0.551	0.550	0.543	0.541	0.538	0.539	0.534
1.5	0.578	0.572	0.564	0.557	0.555	0.547	0.545	0.543	0.542	0.536
2.0	0.629	0.615	0.596	0.566	0.557	0.545	0.543	0.541	0.541	0.538
2.5	0.724	0.697	0.670	0.633	0.598	0.540	0.528	0.519	0.523	0.517
3.0	0.798	0.795	0.773	0.742	0.721	0.651	0.616	0.585	0.572	0.545
4.0	0.857	0.857	0.853	0.845	0.840	0.817	0.811	0.796	0.785	0.722
5.0	0.928	0.927	0.920	0.912	0.905	0.874	0.861	0.857	0.850	0.826
6.0	1.031	1.028	1.018	1.006	0.999	0.959	0.935	0.913	0.920	0.893

Table 9
Surface Mass Fractions of Selected Isotopes for Models with $Z = 1.0 \times 10^{-2}$ at Different Evolutionary Phases (Initial, after FDU, after SDU)

Isot.	Phase	1.3	1.5	2.0	2.5	3.0	4.0	5.0	6.0
^{4}He	INI	2.65E−01	2.65E−01	2.65E−01	2.65E−01	2.65E−01	2.65E−01	2.65E−01	2.65E−01
^{4}He	FDU	2.88E−01	2.84E−01	2.77E−01	2.79E−01	2.81E−01	2.76E−01	2.71E−01	2.70E−01
^{4}He	SDU	⋯	⋯	⋯	⋯	⋯	2.85E−01	3.11E−01	3.31E−01
^{12}C	INI	1.64E−03	1.64E−03	1.64E−03	1.64E−03	1.64E−03	1.64E−03	1.64E−03	1.64E−03
^{12}C	FDU	1.19E−03	1.12E−03	1.01E−03	9.60E−04	9.55E−04	9.72E−04	9.87E−04	9.92E−04
^{12}C	SDU	⋯	⋯	⋯	⋯	⋯	9.34E−04	9.13E−04	8.93E−04
^{13}C	INI	1.99E−05	1.99E−05	1.99E−05	1.99E−05	1.99E−05	1.99E−05	1.99E−05	1.99E−05
^{13}C	FDU	4.96E−05	4.95E−05	4.71E−05	4.65E−05	4.61E−05	4.81E−05	4.92E−05	4.97E−05
^{13}C	SDU	⋯	⋯	⋯	⋯	⋯	4.81E−05	4.74E−05	4.56E−05
^{14}N	INI	5.31E−04	5.31E−04	5.31E−04	5.31E−04	5.31E−04	5.31E−04	5.31E−04	5.31E−04
^{14}N	FDU	1.02E−03	1.11E−03	1.24E−03	1.43E−03	1.52E−03	1.49E−03	1.42E−03	1.40E−03
^{14}N	SDU	⋯	⋯	⋯	⋯	⋯	1.59E−03	1.72E−03	1.89E−03
^{15}N	INI	2.09E−06	2.09E−06	2.09E−06	2.09E−06	2.09E−06	2.09E−06	2.09E−06	2.09E−06
^{15}N	FDU	1.43E−06	1.28E−06	1.04E−06	9.50E−07	9.34E−07	9.97E−07	9.82E−07	9.68E−07
^{15}N	SDU	⋯	⋯	⋯	⋯	⋯	9.48E−07	9.03E−07	8.82E−07
^{16}O	INI	4.40E−03	4.40E−03	4.40E−03	4.40E−03	4.40E−03	4.40E−03	4.40E−03	4.40E−03
^{16}O	FDU	4.40E−03	4.39E−03	4.37E−03	4.23E−03	4.13E−03	4.15E−03	4.20E−03	4.23E−03
^{16}O	SDU	⋯	⋯	⋯	⋯	⋯	4.09E−03	3.96E−03	3.81E−03
^{17}O	INI	1.74E−06	1.74E−06	1.74E−06	1.74E−06	1.74E−06	1.74E−06	1.74E−06	1.74E−06
^{17}O	FDU	3.20E−06	6.12E−06	2.34E−05	2.23E−05	1.82E−05	1.43E−05	1.26E−05	1.17E−05
^{17}O	SDU	⋯	⋯	⋯	⋯	⋯	1.49E−05	1.24E−05	1.10E−05
^{18}O	INI	9.92E−06	9.92E−06	9.92E−06	9.92E−06	9.92E−06	9.92E−06	9.92E−06	9.92E−06
^{18}O	FDU	8.20E−06	7.78E−06	7.08E−06	6.76E−06	6.69E−06	6.58E−06	6.66E−06	6.69E−06
^{18}O	SDU	⋯	⋯	⋯	⋯	⋯	6.35E−06	6.16E−06	5.99E−06
^{23}Na	INI	2.58E−05	2.58E−05	2.58E−05	2.58E−05	2.58E−05	2.58E−05	2.58E−05	2.58E−05
^{23}Na	FDU	2.64E−05	2.78E−05	3.18E−05	3.42E−05	3.50E−05	3.47E−05	3.41E−05	3.41E−05
^{23}Na	SDU	⋯	⋯	⋯	⋯	⋯	3.60E−05	3.78E−05	4.09E−05

for instance, in low-metallicity stars (Gratton et al. 2000) and measured in oxide grains (Al₂O₃) of group 1 (Nittler et al. 1997). Considering that, to date, no definitive theoretical recipe exists for this non-convective mixing, our models do not include any RGB extra mixing. Among the isotopes reported in Tables 9 and 10, the most sensitive isotopes to an extra-mixing process should be ^{13}C and ^{18}O. This should be kept in mind when adopting our isotopic abundances.

4. THE TP-AGB PHASE (I): PHYSICS

FUNS models with mass $1.3 \leqslant M/M_\odot \leqslant 3.0$ were extensively analyzed in Cristallo et al. (2009) and Cristallo et al. (2011). However, in order to provide a general picture of stellar evolution during the AGB phase, some of their physical properties will again be addressed here. In order to evaluate the behavior of the TDU mechanism as a function of the mass and the metallicity, we plot the ratio between the mass of H-depleted dredged-up material at each TDU (δM_{TDU}) and the envelope mass as a function of the mass of the H-exhausted core in Figure 3. Such a quantity provides an estimate of the TDU efficiency in polluting the convective envelope. This figure shows that at $Z = 10^{-2}$ (upper panel), a star with initial mass $M = 1.3\ M_\odot$ is close to the lower mass limit to experience TDU. The maximum TDU efficiency is reached for the 3 $M_\odot$ model. Then, there is an abrupt drop in TDU efficiency corresponding to the 4 $M_\odot$ model. In fact, the physical structure of this model is deeply different with respect to those of lower masses. In particular, the mass of the
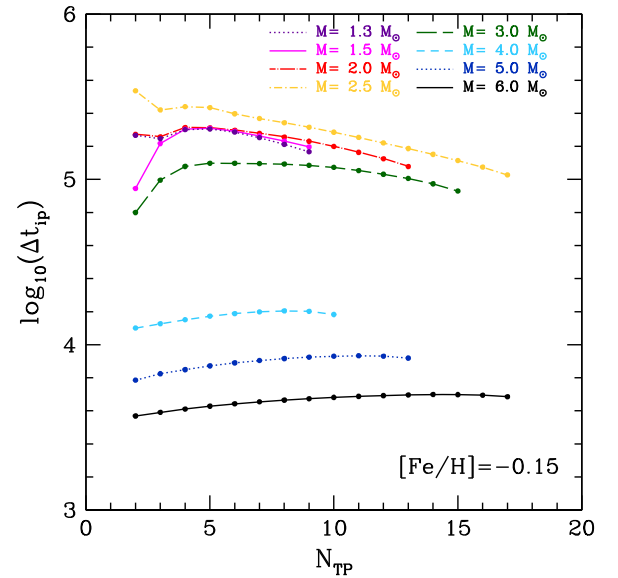
Table 10
Surface Mass Fractions of Selected Isotopes for Models with $Z = 2.3 \times 10^{-4}$ at Different Evolutionary Phases (Initial, after FDU, after SDU)

Isot.	Phase	1.3	1.5	2.0	2.5	3.0	4.0	5.0	6.0
^{4}He	INI	2.45E−01	2.45E−01	2.45E−01	2.45E−01	2.45E−01	2.45E−01	2.45E−01	2.45E−01
^{4}He	FDU	2.68E−01	2.69E−01	2.66E−01	2.46E−01	...	...	...	...
^{4}He	SDU	...	...	...	2.55E−01	2.63E−01	3.03E−01	3.28E−01	3.42E−01
^{12}C	INI	1.68E−05	1.68E−05	1.68E−05	1.68E−05	1.68E−05	1.68E−05	1.68E−05	1.68E−05
^{12}C	FDU	1.13E−05	1.02E−05	8.62E−06	1.44E−05	...	...	...	...
^{12}C	SDU	...	...	...	8.76E−06	8.03E−06	7.13E−06	6.71E−06	1.06E−05
^{13}C	INI	2.04E−07	2.04E−07	2.04E−07	2.04E−07	2.04E−07	2.04E−07	2.04E−07	2.04E−07
^{13}C	FDU	4.93E−07	4.75E−07	4.52E−07	7.55E−07	...	...	...	...
^{13}C	SDU	...	...	...	4.75E−07	4.58E−07	4.41E−07	4.27E−07	4.17E−07
^{14}N	INI	5.44E−06	5.44E−06	5.44E−06	5.44E−06	5.44E−06	5.44E−06	5.44E−06	5.44E−06
^{14}N	FDU	1.16E−05	1.29E−05	1.85E−05	7.60E−06	...	...	...	...
^{14}N	SDU	...	...	...	1.83E−05	2.18E−05	3.16E−05	3.90E−05	4.33E−05
^{15}N	INI	2.14E−08	2.14E−08	2.14E−08	2.14E−08	2.14E−08	2.14E−08	2.14E−08	2.14E−08
^{15}N	FDU	1.38E−08	1.23E−08	1.06E−08	1.41E−08	...	...	...	...
^{15}N	SDU	...	...	...	9.51E−09	8.59E−09	7.59E−09	6.98E−09	6.63E−09
^{16}O	INI	1.42E−04	1.42E−04	1.42E−04	1.42E−04	1.42E−04	1.42E−04	1.42E−04	1.42E−04
^{16}O	FDU	1.42E−04	1.42E−04	1.33E−04	1.42E−04	...	...	...	...
^{16}O	SDU	...	...	...	1.37E−04	1.34E−04	1.23E−04	1.16E−04	1.11E−04
^{17}O	INI	1.79E−08	1.79E−08	1.79E−08	1.79E−08	1.79E−08	1.79E−08	1.79E−08	1.79E−08
^{17}O	FDU	2.18E−07	9.38E−07	2.39E−06	1.85E−08	...	...	...	...
^{17}O	SDU	...	...	...	7.97E−07	1.44E−06	1.98E−06	1.77E−06	1.52E−06
^{18}O	INI	1.02E−07	1.02E−07	1.02E−07	1.02E−07	1.02E−07	1.02E−07	1.02E−07	1.02E−07
^{18}O	FDU	7.59E−08	6.94E−08	5.38E−08	9.70E−08	...	...	...	...
^{18}O	SDU	...	...	...	6.04E−08	5.55E−08	4.88E−08	4.52E−08	8.00E−08
^{23}Na	INI	2.64E−07	2.64E−07	2.64E−07	2.64E−07	2.64E−07	2.64E−07	2.64E−07	2.64E−07
^{23}Na	FDU	2.94E−07	3.35E−07	3.98E−07	2.64E−07	...	...	...	...
^{23}Na	SDU	...	...	...	4.26E−07	7.28E−07	1.69E−06	2.13E−06	2.12E−06
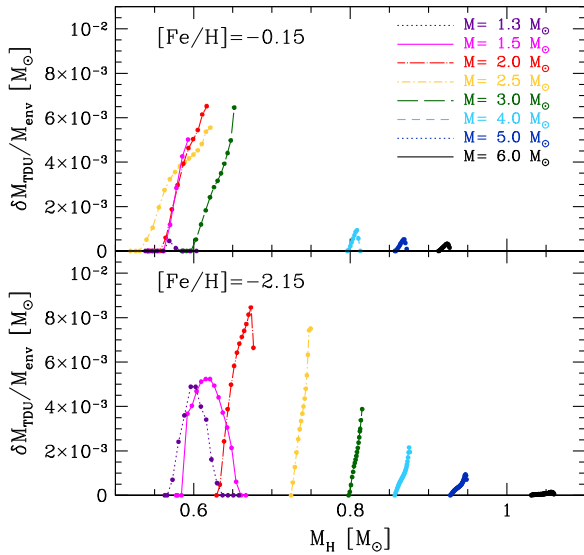
Figure 3. Ratio between the mass of H-depleted dredged-up material (δM_{TDU}) and the envelope mass (M_{env}) for different masses at $Z = 10^{-2}$ (upper panel) and $Z = 2.4 \times 10^{-4}$ (lower panel).

Figure 4. Interpulse duration for models with $Z = 10^{-2}$.

H-exhausted core (M_H) is definitely larger. This implies a larger compression of the H-exhausted layers, and thus the He-intershell is thinner and hotter. Consequently, the time needed to reach the ignition conditions for the 3α process during

H-shell burning is shorter. Hence, the interpulse period decreases and, finally, the TDU efficiency is lower (Straniero et al. 2003a). In Figure 4, we report the interpulse phase duration (Δt_{ip}) for models with $Z = 10^{-2}$. While for models

with $M \leqslant 3\,M_\odot$ the $\Delta t_{\rm ip} \geqslant 10^5$, it decreases to 10^4 years and 5000 years for larger masses $4\,M_\odot$ and $6\,M_\odot$, respectively. As shown in the lower panel of Figure 3, at low metallicities, even the lowest masses (1.3–1.5 $M_\odot$) experience a deep TDU due to the low CNO elemental abundances in the envelope (which implies a reduced H-shell efficiency). Moreover, the transition between LMS-AGBs and IMS-AGBs is smoother, as the 2.5 and 3.0 $M_\odot$ models begin the TP-AGB phase with definitely larger core masses with respect to their high-metallicity counterparts. More massive models (4–5–6 $M_\odot$) are characterized by a very low TDU efficiency (as their metal-rich counterparts), but show a definitely larger number of TPs (see Table 11). This is due to the fact that the stellar structure is more compact, and thus the external layers are hotter. As a consequence, the mass loss erodes the convective envelope at a lower rate and the star experiences a larger number of TPs. In Figure 5, we report the $\delta M_{\rm TDU}$ for all of the computed IMS-AGB models. As already noted, in the 6 $M_\odot$ model there is no trend with the initial metallicity, as the TDU efficiency is always very low. In the 5 $M_\odot$ models, there is a slight increase of TDU efficiency at low metallicities. For $Z \leqslant Z_\odot$, the 4 $M_\odot$ models show a clear increase of TDU efficiency with decreasing initial iron content. The $Z = 2 \times 10^{-2}$ model represents an exception because it shows a net increase of the TDU efficiency. In fact, the core at the beginning of TP-AGB is less massive than that of models with lower Z, and thus an increase of the TDU efficiency is expected. In Table 12, we report the cumulative dredged-up mass (in $M_\odot$) for different initial masses and metallicities ($\Delta M_{\rm TDU}$). As expected, models with the largest $\Delta M_{\rm TDU}$ are in the range 2–2.5 $M_\odot$, and thus the major pollution of the interstellar medium is expected from these objects (see Section 6). Another way to evaluate the TDU efficiency is to analyze the behavior of the λ values, defined as the ratios between the mass of H-depleted dredged-up material and the mass growth of the H-exhausted core during the previous interpulse phase (see Figures 6 and 7). At solar-like metallicities, the maximum value of λ we obtain is ~ 0.5 for stars with $M \geqslant 2.0\,M_\odot$. At low Z, instead, λ grows to 0.8, implying a larger TDU efficiency.

Depending on the final C/O ratio, stars are classified as C-rich objects (C/O > 1) or O-rich objects (C/O < 1). The final surface C/O ratio depends on many factors whose effects are not easily disentangled. Among these factors, the TDU efficiency and the mass-loss rate play major roles. The uncertainties affecting these phenomena have been extensively reviewed in Ventura & D'Antona (2005a, 2005b). They show that very different results can be obtained by modifying, within uncertainties, the recipe adopted to treat them. In Section 7, we will compare our models to similar computations described in recent literature.

While the TDU efficiency is strictly connected to the mixing algorithms adopted to compute the models (mixing scheme; treatment of convective borders; etc.), the number of TDUs mainly depends on the mass-loss mechanism. The latter, in fact, erodes the mass of the convective envelope and determines the dilution factor between the cumulative dredge up material and the envelope mass itself. Thus, if the envelope mass is not too large and the number of experienced TDUs is high enough, then the model shows C/O > 1 at the surface. Once again, the duration of the C-rich phase depends on the efficiency of mass loss in eroding the convective envelope. As already stressed, the presence of carbon bearing molecules

locally increases the opacity. Thus, we expect an increase of the mass-loss rate when the C/O becomes greater than 1.

In Table 13, we report the total TP-AGB lifetimes ($\tau_{\rm TP-AGB}$) and the percentage spent in the C-rich regime. As can be seen, all of the models become C-rich at low metallicities and spend the majority of their TP-AGB lifetime in the C-rich regime. This can also be appreciated in Figure 8 where we report $\tau_{\rm TP-AGB}$ (histograms) and the corresponding time spent during the C-rich regime (shaded histograms) for three different metallicities ($Z = 2 \times 10^{-2}$: upper panel; $Z = 6 \times 10^{-3}$: middle panel; $Z = 1 \times 10^{-3}$: lower panel). In general, the larger the metallicity, the longer the TP-AGB lifetimes and the lower the time fraction spent in the C-rich regime. The lifetimes of IMS-AGBs are definitely shorter (about a factor 10) with respect to LMS-AGBs. From Figure 8, it turns out that stars with the longest TP-AGB lifetimes have $M = 2.5\,M_\odot$ for large and intermediate metallicities. At low Z, instead, we find a monotonic trend with the lowest masses showing the longest $\tau_{\rm TP-AGB}$.

Note that the HBB and H-TDU could be at work during the TP-AGB phase. Both phenomena are able to modify the surface C/O ratio. In Figure 9, we report the maximum temperature attained at the base of the convective envelope during the TP-AGB phase of 6 $M_\odot$ models at different metallicities. In order to efficiently activate the HBB, the base of the convective envelope should reach 80 MK. In our models, this condition is fulfilled at the lowest metallicities for the largest masses (5–6 $M_\odot$) only. Another interesting phenomenon, possibly working during the TP-AGB phase, is H-TDU. In this case, the temperature at the base of the convective envelope is high enough to restart H burning during a TDU episode. As a result, protons are mixed and burnt on-flight. In our models, H-TDU is activated at low metallicities only, with particularly high efficiencies in the more massive models. The effects of HBB and H-TDU on the nucleosynthesis of our models are discussed in Section 6. Considering that the envelopes of AGB stars are highly expanded ($R \sim 200$–1000 $R_\odot$) and that the average convective velocity is low ($v \sim 10^5$ cm s^{-1}), for some isotopes the convective turnover timescale is longer than the proton capture timescales at the base of the convective envelope. In order to properly treat those processes, computation of the chemical evolution should be performed by coupling mixing and burning. We intend to address it in a future study. Models presented in this paper have been calculated with a three-step process. First, we burn chemicals over a model time step. Then, we mix them in convective regions following a time-dependent mixing scheme derived from an algorithm proposed[9] by Sparks & Endal (1980). Finally, we again burn chemicals in convective regions for only a fraction (10^{-2}) of the model time step. This is done in order to allow isotopes to reach their equilibrium abundance if their burning timescale is lower than the convective turnover timescale.

Another interesting feature of IMS-AGB models is the large temperature reached at the bottom of the convective shells generated by TPs ($T_{\rm max}^{\rm TP}$). Depending on $T_{\rm max}^{\rm TP}$, the ^{22}Ne(α, n)^{25}Mg reaction can be efficiently activated. This can lead to a second neutron burst (additional to that from the ^{13}C(α,n)^{16}O reaction) with important consequences for the s-process nucleosynthesis (see Section 6). From an inspection of

---

[9] We assume that neutrons are in local equilibrium, and hence they are not mixed.

Table 11

Description of Dredge Up Events: First Dredge up (F), Second Dredge Up (S), and Third Dredge Up (T) Characterizing Models with Different Masses and Metallicities (if the model experiences third dredge up, we report the number of experienced episodes)

[Fe/H]	−2.15			−1.67			−1.15			−0.85			−0.67			−0.37			0.24			−0.15			0.00			0.15		
Mass	F	S	T	F	S	T	F	S	T	F	S	T	F	S	T	F	S	T	F	S	T	F	S	T	F	S	T	F	S	T
1.3	YES	NO	9	YES	NO	7	YES	NO	5	YES	NO	5	YES	NO	4	YES	NO	3	YES	NO	2	YES	NO	2	YES	NO	NO	YES	NO	NO
1.5	YES	NO	12	YES	NO	9	YES	NO	8	YES	NO	7	YES	NO	6	YES	NO	7	YES	NO	5	YES	NO	4	YES	NO	5	YES	NO	4
2.0	YES	NO	13	YES	NO	13	YES	NO	11	YES	NO	11	YES	NO	11	YES	NO	10	YES	NO	10	YES	NO	9	YES	NO	9	YES	NO	9
2.5	YES	YES	14	YES	YES	11	YES	YES	10	YES	NO	10	YES	YES	11	YES	NO	13	YES	NO	15	YES	NO	14	YES	NO	13	YES	NO	15
3.0	NO	YES	16	YES	YES	13	YES	YES	11	YES	YES	10	YES	YES	9	YES	YES	9	YES	YES	10	YES	NO	11	YES	NO	13	YES	NO	14
4.0	NO	YES	25	YES	YES	19	YES	YES	15	YES	YES	15	YES	YES	12	YES	YES	9	YES	YES	9	YES	YES	8	YES	YES	8	YES	YES	8
5.0	NO	YES	39	NO	YES	32	YES	YES	24	YES	YES	22	YES	YES	18	YES	YES	12	YES	YES	11	YES	YES	11	YES	YES	8	YES	YES	7
6.0	NO	YES	82	NO	YES	66	NO	YES	57	YES	YES	41	YES	YES	31	YES	YES	22	YES	YES	18	YES	YES	16	YES	YES	15	YES	YES	11
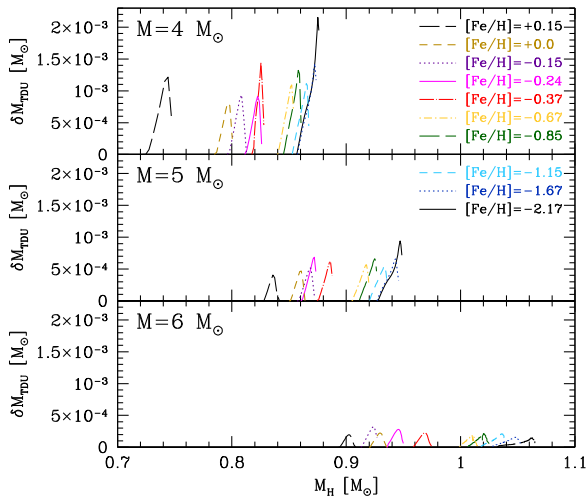
Figure 5. Mass of H-depleted dredged-up material at each TDU for models with initial mass $M = 4\ M_\odot$ (upper panel), $M = 5\ M_\odot$ (middle panel), and $M = 6\ M_\odot$ (lower panel).

Figures 10 and 11, it can be noted that during the AGB, $T_{\mathrm{max}}^{\mathrm{TP}}$ progressively increases, reaches a maximum, and then slightly decreases. This quantity depends on the core mass, the envelope mass, and the metallicity (see Straniero et al. 2003a). As $T_{\mathrm{max}}^{\mathrm{TP}}$ scales with the core mass, we expect the largest temperatures to be attained in those models with the largest initial masses. This is clearly shown in Figure 10 where it can be seen that low-mass stars barely reach $T_{\mathrm{max}}^{\mathrm{TP}} \sim 3 \times 10^8$ K, while IMS-AGB easily go beyond this limit. The dependence on the initial metallicity is also evident; the models with low Z show definitely larger $T_{\mathrm{max}}^{\mathrm{TP}}$ (up to 3.8×10^8 K) with respect to their solar-like metallicity counterpart. At [Fe/H] = −2.15, the absolute maximum temperature is reached in the 5 $M_\odot$ model and not in the 6 $M_\odot$ model. In this case, a larger mass of the H-exhausted core (which implies higher $T_{\mathrm{max}}^{\mathrm{TP}}$) cannot compensate the decrease of the duration of the interpulse phases.

5. pH-FRUITY: A NEW WEB PHYSICAL INTERFACE

The FRUITY database (Cristallo et al. 2011) is organized under a relational model through the MySQL Database Management System. Its web interface allows users to submit query strings resulting from appropriately filling out the fields to the managing system specifying the initial mass, metallicity, and rotational velocity. To date, FRUITY has included our predictions for the surface composition of AGB stars and the stellar yields they produce. For each model, different types of tables can be downloaded (elemental and isotopic surface compositions; net and total yields; s-process indexes). In this work, we add a new module (ph-FRUITY) containing the physical quantities of interest characterizing AGB models. The downloadable quantities (given for each TP, with and without TDU) are the absolute age, the duration of the previous interpulse phase (Δt_{ip}), the total mass (M_{tot}), the mass of the H-exhausted core (M_{H}), the dredged-up mass (δM_{TDU}), the λ quantity, the maximum temperature attained at the bottom of the convective zone generated by the TP ($T_{\mathrm{max}}^{\mathrm{TP}}$), the mean bolometric magnitude of the previous interpulse period ($M_{\mathrm{bol}} = 4.75 - 2.5 * \log L/L_\odot$), the logarithm of the mean surface temperature of the previous interpulse period ($\log T_{\mathrm{eff}}$),

and the logarithm of the mean surface gravity of the previous interpulse[10] period ($\log g$). Note that we stop the calculations once the TDU has stopped operating. However, the core mass continues to grow until the nearly complete erosion of the convective envelope by the strong stellar winds. Such an occurrence is accounted for by providing a set of key extrapolated physical quantities (labeled as *EXTRA*). First, we calculate the mass lost in the wind and the growth of the H-exhausted core during the previous interpulse phase. Then, we extrapolate them by means of a fifth-order polynomial. Then, we derive other tabulated quantities (Δt_{ip}, M_{bol}, $\log T_{\mathrm{eff}}$, and $\log g$). Following the original FRUITY philosophy, those quantities can be downloaded in a "Multiple case format" (the query returns multiple tables, depending on the number of selected models) or in a "Single case format" (the query returns a single table containing all the selected models).

6. THE TP-AGB PHASE (II): NUCLEOSYNTHESIS

The nucleosynthesis occurring during the TP-AGB phase is extremely rich. In fact, many types of nuclear processes are at work, including strong force reactions (proton captures, neutron captures, α captures) and weak force reactions (β decays, electron captures). Nearly all of the isotopes in the periodic table are affected, apart from Trans-uranic species. The nucleosynthetic details related to the evolution of low-mass TP-AGB stars have already been presented in Cristallo et al. (2009) and Cristallo et al. (2011). As we have already stressed, the final surface abundances and, consequently, the net yields are slightly smaller with respect to data presented in those two papers due to a previous underestimate of the opacities in the most external layers of the star. The proper opacities imply lower surface temperatures, and thus higher mass-loss rates. Consequently, models experience a reduced number of TDU episodes. However, s-process indexes are not affected by this problem (see Section 6), and thus most of the conclusions derived in Cristallo et al. (2011) are still valid.

In Figure 12, we report the final surface chemical distributions[11] for the whole mass range and two selected metallicities ($Z = 10^{-2}$: upper panel; $Z = 2.4 \times 10^{-4}$: lower panel). At large Z, we note a net production of carbon in LMS-AGBs only. The 4 and 5 $M_\odot$ models present a slight final surface increase, while the 6 $M_\odot$ model destroys it (due to the occurrence of the FDU, the SDU, and to a low TDU efficiency). At low metallicity, all of the models show consistent production of ^{12}C. In Figure 13, we report the final surface number ratios N(^{12}C)/N(^{56}Fe) and N(^{13}C)/N(^{56}Fe) as a function of the initial metallicity for the whole FRUITY set (upper and middle panels, respectively). There is a clear increase in ^{12}C production as the initial iron content decreases. The same is not true for ^{13}C, which is efficiently synthesized by the more massive AGBs and for [Fe/H] < −0.5 only. The (^{13}C/^{56}Fe) ratio is in fact nearly flat for models with M < 2.5 $M_\odot$. For larger masses (5–6 $M_\odot$), instead, there is net ^{13}C production due to the simultaneous occurrence of HBB and H-TDU. The corresponding increase of ^{14}N can be observed in Figure 14 (upper panel) in addition to the decrease of the ^{12}C/^{13}C ratio (lower panel of Figure 13). We note that the ^{13}C

---

[10] Those quantities are weighted averages on time.
[11] In the usual spectroscopic notation: [X$_i$/Fe] = log (N(X$_i$)/N(Fe))$_*$ − log (N (X$_i$)/N(Fe))$_\odot$. Models with initial masses $M = 1.3$, $M = 1.5$, and $M = 2.5\ M_\odot$ are omitted for clarity.

Table 12
Cumulative Dredged-up Mass (in $M_\odot$) for Different Initial Masses and Metallicities

Mass/[Fe/H]	−2.15	−1.67	−1.15	−0.85	−0.67	−0.37	−0.24	−0.15	0.00	0.15
1.3	1.36E−02	1.19E−02	9.89E−03	8.64E−03	4.65E−03	2.82E−03	5.75E−04	2.64E−04	0.00E+00	0.00E+00
1.5	3.28E−02	2.83E−02	2.45E−02	2.14E−02	1.64E−02	1.41E−02	8.15E−03	8.46E−03	6.66E−03	5.58E−03
2.0	7.89E−02	6.44E−02	6.54E−02	6.15E−02	5.26E−02	4.61E−02	3.50E−02	3.88E−02	2.91E−02	2.96E−02
2.5	6.61E−02	4.54E−02	5.88E−02	6.12E−02	6.40E−02	8.20E−02	7.23E−02	7.25E−02	5.91E−02	6.67E−02
3.0	4.83E−02	2.95E−02	3.17E−02	3.20E−02	2.72E−02	4.10E−02	4.74E−02	5.77E−02	6.01E−02	6.43E−02
4.0	5.15E−02	3.15E−02	2.17E−02	2.27E−02	1.59E−02	1.53E−02	8.90E−03	8.59E−03	7.28E−03	1.10E−02
5.0	4.31E−02	3.01E−02	2.16E−02	2.15E−02	1.52E−02	9.38E−03	9.80E−03	7.62E−03	5.71E−03	4.06E−03
6.0	1.64E−02	1.77E−02	1.84E−02	1.26E−02	9.32E−03	8.36E−03	8.61E−03	8.47E−03	5.52E−03	3.65E−03
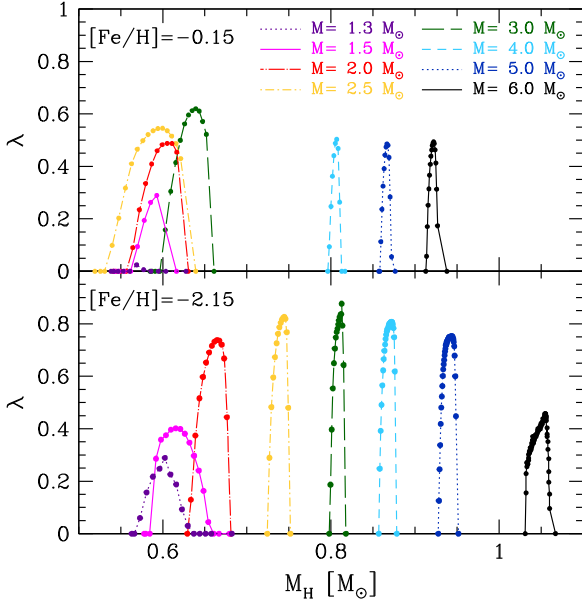
Figure 6. Same as in Figure 3, but for the λ values defined as the ratio between the mass of H-depleted dredged-up material and the growth of the H-exhausted core during the previous interpulse phase.
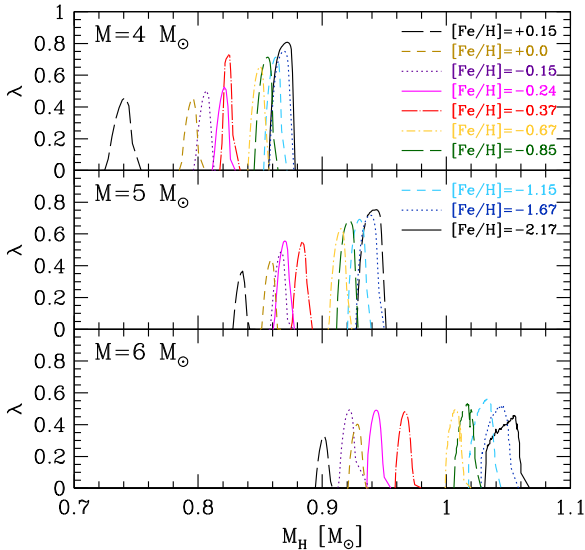
Figure 7. Same as in Figure 5, but for λ values.

production is affected by the presence of non-canonical mixing during the RGB phase, as already stressed in Section 3.

The solar oxygen abundance mainly consists of ^{16}O. Its production is null at large metallicities, while there is a net production for the whole mass range at low Z, thanks to TDU episodes which mix to the surface ^{16}O. The latter is synthesized by the ^{12}C$(\alpha,\gamma)^{16}$O reactions during TPs and, to a lesser extent, by the ^{13}C$(\alpha,n)^{16}$O reaction during radiative ^{13}C burning. The other oxygen isotopes (^{17}O and ^{18}O) exhibit completely different behaviors. The ^{17}O abundance results from the equilibrium between the production channel (^{16}O(p,$\gamma)^{17}$F $(\beta^+)^{17}$O nuclear chain) and the destruction channel (^{17}O(p, $\alpha)^{14}$N reaction). Its surface abundance depends on the depth of convection in regions with an ^{17}O profile, i.e., those experiencing incomplete CNO burning. For fixed [Fe/H], we find the highest ^{16}O/^{17}O for the lowest masses (middle panel in Figure 14), thus confirming the values already reported in the literature (see, e.g., Lebzelter et al. 2015). The complex interplay between mixing and burning does not allow us to identify a common behavior with the metallicity. However, the models show slightly larger ^{16}O/^{17}O ratios at large metallicities. The more neutron rich oxygen isotope (^{18}O) behaves very differently (see lower panel of 14). This isotope is mainly produced by the ^{14}N$(\alpha,\gamma)^{18}$F$(\beta^+)^{18}$O nuclear chain, while it is destroyed by the ^{18}O(p,$\alpha)^{15}$N and ^{18}O$(\alpha,\gamma)^{22}$Ne reactions. The ^{16}O/^{18}O ratio is nearly constant for all masses and [Fe/H] $\geqslant -1.15$. At low metallicities, its increase is due to the dredge up of primary ^{16}O, as explained before. Thus, in our models, ^{18}O is basically untouched. This would not be the case if we were to consider the effects induced by non-convective mixing during the RGB and the AGB phases. In fact, it has been demonstrated that the inclusion of this kind of mixing strongly affects the surface ^{18}O abundance of low-mass stars and that this is needed to fit laboratory measurements of oxygen isotopic ratios in pre-solar SiC grains (see Palmerini et al. 2011). Those small dust particles are trapped in primitive meteorites and currently provide the most severe constraints for AGB nucleosynthesis (see, e.g., Liu et al. 2014, 2015).

The fluorine nucleosynthesis is extremely complex, since it involves both neutron and proton captures (see Abia et al. 2009, 2010, 2011). ^{19}F is very sensitive to a variation of the initial stellar mass (see lower panel of Figure 12). Its production basically depends on the amount of ^{15}N in the He-intershell, which in turn is correlated to the amount of ^{13}C in the ashes of the H-burning shell, as well as in the ^{13}C pocket (see the discussion in Cristallo et al. 2014). In IMS-AGBs, fluorine production is strongly suppressed due to the reduced contribution from the radiative ^{13}C burning and from the increased efficiency of ^{19}F destruction channels (the ^{19}F(p, $\alpha)^{16}$O reaction and, above all, the ^{19}F$(\alpha,p)^{22}$Ne reaction).

Neon is enhanced in all of the models experiencing TDU, due to the dredge up of freshly synthesized ^{22}Ne during TPs via

Table 13
TP-AGB Lifetimes (in Units of 10^4 yr) and Percentage Spent in the C-rich Regime for Different Initial Masses and Metallicities

[Fe/H] Mass	−2.15		−1.67		−1.15		−0.85		−0.67		−0.37		0.24		−0.15		0.00		0.15	
	τ	C(%)	τ	C(%)	τ	C(%)	τ	C(%)	τ	C(%)	τ	C(%)	τ	C(%)	τ	C(%)	τ	C(%)	τ	C(%)
1.3	176	79	191	62	180	57	181	57	175	47	166	25	170	0	170	0	152	0	156	0
1.5	163	74	171	71	160	62	182	53	173	48	175	41	181	33	150	10	156	0	183	0
2.0	129	84	125	77	134	79	202	68	213	60	226	45	219	35	219	38	206	24	202	11
2.5	64.0	89	69.1	84	70.2	83	108	76	147	67	283	59	313	47	335	44	296	34	316	26
3.0	36.5	86	29.2	80	28.7	80	37.1	69	38.6	64	80.5	47	112	44	161	36	187	28	240	20
4.0	27.1	91	22.6	78	16.0	79	17.0	66	13.9	49	13.5	32	13.1	0	13.9	0	14.0	0	26.3	0
5.0	20.6	90	16.6	79	12.3	75	12.1	65	10.6	43	10.0	0	10.6	0	10.2	0	9.7	0	10.4	0
6.0	9.7	76	10.5	65	9.6	69	7.6	52	6.4	34	7.3	0	7.6	0	7.8	0	7.2	0	6.9	0
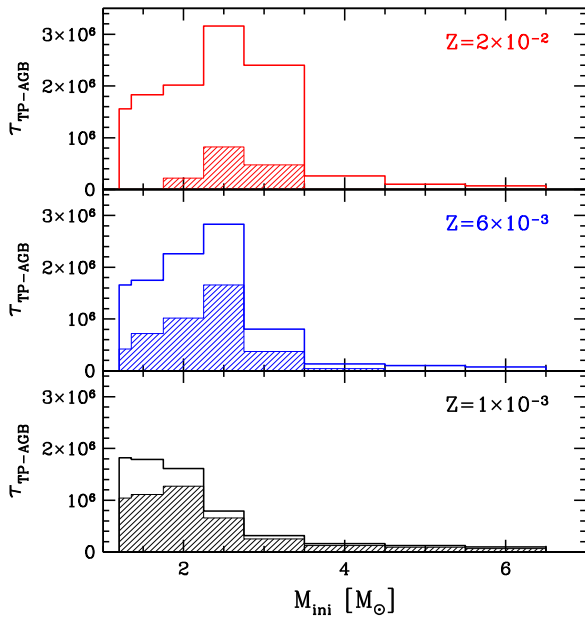
Figure 8. TP-AGB lifetimes for three selected metallicities. Shaded histograms refer to the C-rich phase of the models.
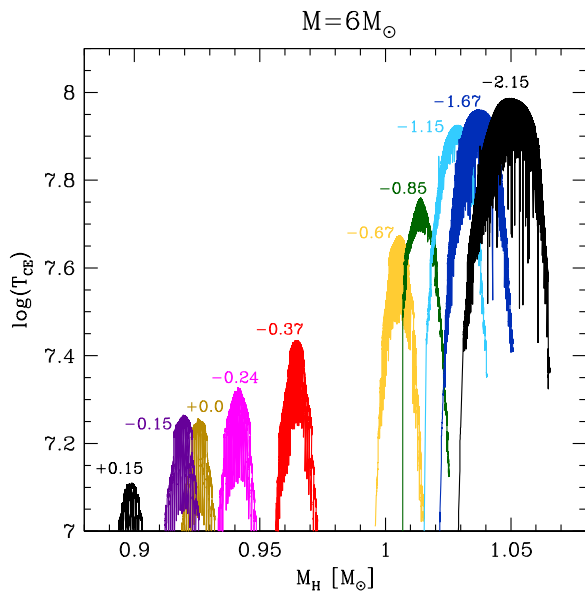
Figure 9. Evolution of the temperature attained at the base of the convective envelope during the TP-AGB phase of 6 $M_\odot$ models at different [Fe/H].


Figure 10. As in Figure 3, but for the maximum temperature attained at the bottom of the convective zone generated by a TP.
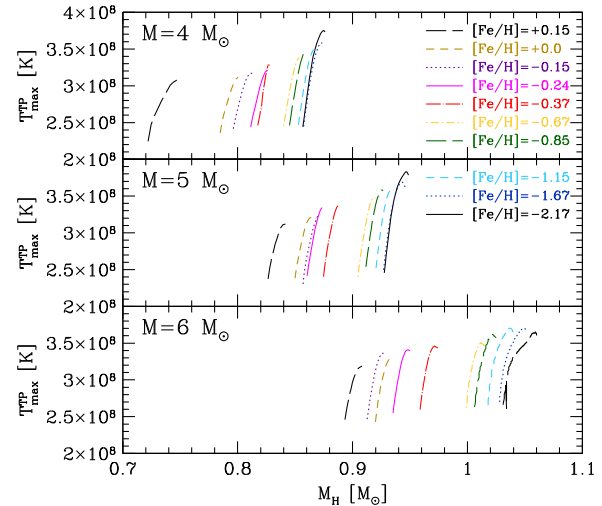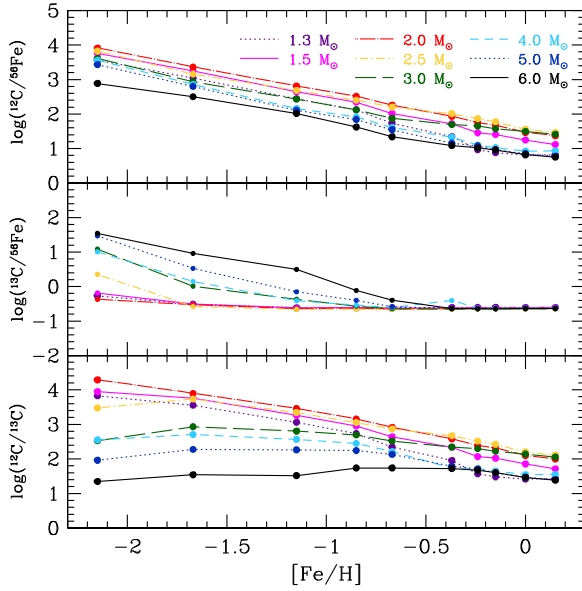

Figure 11. As in Figure 5, but for the maximum temperature attained at the bottom of the convective zone generated by a TP.

a double α capture on the abundant ^{14}N. Its abundance directly affects the ^{23}Na nucleosynthesis. In LMS-AGBs, sodium can be synthesized through proton captures during the formation of the ^{13}C pocket, as well as through neutron captures during both the radiative burning of the ^{13}C pocket and the convective ^{22}Ne-burning in the convective shells generated by TPs (see Cristallo et al. 2009). This leads to a notable ^{23}Na surface enhancement, in particular at low metallicities. In more massive stars, the sodium nucleosynthesis is affected by HBB (see, e.g., Ventura & D'Antona 2006; Karakas & Lattanzio 2014). In our models, we find a slight increase of the ^{23}Na surface abundance directly correlated to HBB, which is mildly activated in the more massive low Z models.

In our models, magnesium is enhanced at low metallicities due to an increased production of ^{25}Mg and ^{26}Mg via the ^{22}Ne

(α,n)^{25}Mg and ^{22}Ne(α,γ)^{25}Mg reactions (see upper panel of Figure 15). We find a considerable Mg overabundance at [Fe/H] $\leqslant -2.15$ only (we note that for [Fe/H] $\leqslant -1.67$ we adopt an α-enhanced initial mixture). At low metallicities, both ^{24}Mg/^{25}Mg and ^{24}Mg/^{26}Mg are lower than solar (intermediate panels of Figure 15). Both quantities show a minimum for models with initial mass $M \sim 3\,M_\odot$. Exceptions are represented by the less massive models (1.3 $M_\odot$ and 1.5 $M_\odot$) in which the marginal activation of both the ^{22}Ne(α,n)^{25}Mg and ^{22}Ne(α,γ)^{25}Mg reactions does not compensate for the initial ^{24}Mg enhancement. At intermediate-to-high metallicities, the final surface ^{26}Mg/^{25}Mg ratio of our models is nearly constant (and close to the solar value). At low [Fe/H], instead, it depends on the initial mass, with 2 $M_\odot$ showing the maximum value and 5 $M_\odot$ the minimum value (see lower panel of Figure 15). During TPs, in massive models, the neutron density is large and ^{25}Mg behaves as a neutron poison, thus feeding ^{26}Mg.

The contribution to the overall nucleosynthesis from the ^{13}C (α,n)^{16}O reaction is strongly correlated to the initial mass of
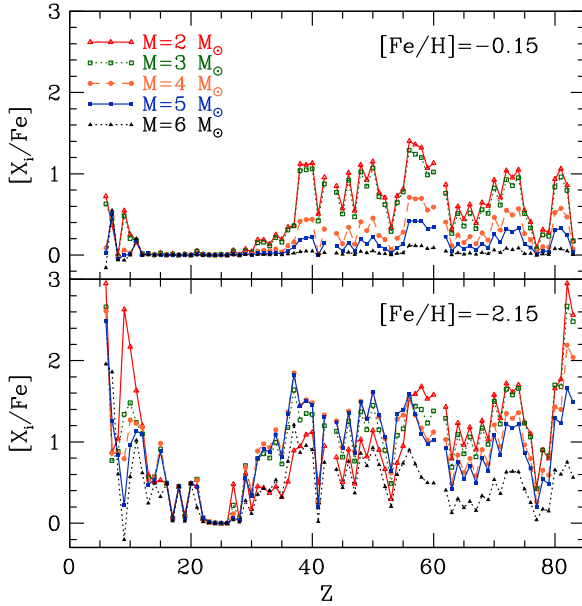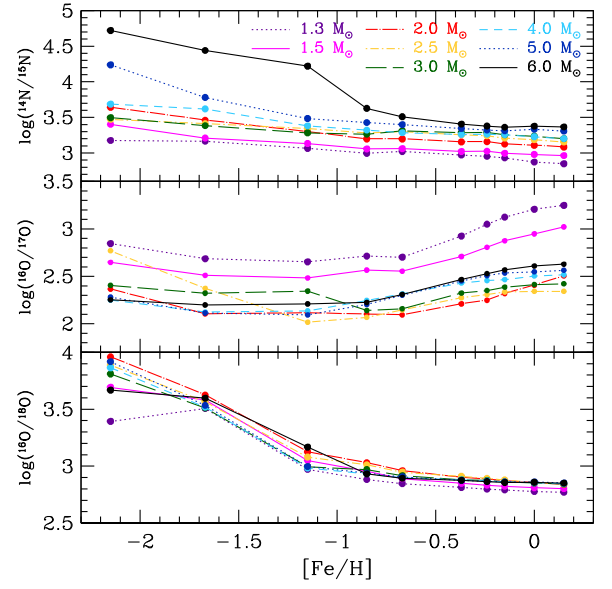
Figure 12. Final element surface distribution for selected masses at solar-like metallicity (upper panel) and low metallicity (lower panel).
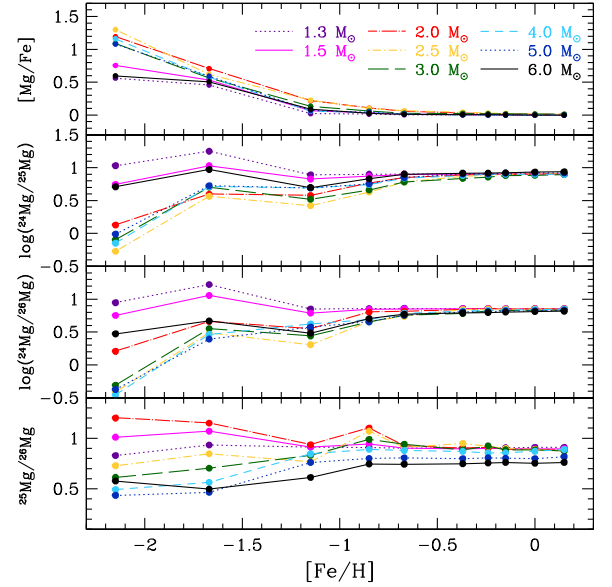

Figure 14. Final surface distributions of the ^{14}N/^{15}N ratio (upper panel), the ^{16}O/^{17}O ratio (middle panel), and the ^{16}O/^{18}O ratio (lower panel).

Figure 13. Final surface distributions of ^{12}C (upper panel) and ^{13}C (middle panel) with respect to ^{56}Fe as a function of the initial metallicity for the whole FRUITY set. Final surface ^{12}C/^{13}C ratios are also reported (lower panel).

Figure 15. Final surface [Mg/Fe] (upper panel), ^{24}Mg/^{25}Mg and ^{24}Mg/^{26}Mg ratios (intermediate panels) and, ^{25}Mg/^{26}Mg ratio (lower panel).

the model. In Cristallo et al. (2009), we showed that the mass extension of the ^{13}C pocket decreases with the TDU number (see also Figure 1 in Cristallo et al. 2011), implying a progressive reduction of the *s*-process efficiency as the star evolves along the AGB. The larger the core mass, the lower the ^{13}C size. Thus, ^{13}C pockets in IMS-AGB models are definitely thinner with respect to those found in LMS-AGBs, due to their definitely larger core masses. In Figure 16, we compare the profiles of the *effective* ^{13}C (defined as X(^{13}C$_{\rm eff}$) = X (^{13}C) − 13/14 * X(^{14}N)) in the pocket after the second TDU for three different models (2.0, 4.0, and 6.0 $M_\odot$) with Z = 10^{-2}. This quantity takes into account the poisoning effect of ^{14}N (via the ^{14}N(n,p)^{14}C reaction), and thus provides a better estimate of the neutrons effectively contributing to the

synthesis of heavy elements (see Cristallo et al. 2009). In Figure 16, the pockets have been manually shifted in mass, while the zero point of the abscissa is arbitrary. The pocket found in the 6 $M_\odot$ model is four times smaller than that found in the 2 $M_\odot$ model due to the shrinking of the He-intershell with increasing initial stellar mass. Moreover, the integrated amount of effective ^{13}C in the pocket decreases by more than a factor of 3, passing from the 2 $M_\odot$ model ($\sum^{13}$ C$_{\rm eff}$ = 7.8 × 10^{-6} $M_\odot$) to the 4.0 $M_\odot$ model ($\sum^{13}$ C$_{\rm eff}$ = 2.2 × 10^{-6} $M_\odot$), and is reduced by another factor of 7 in the 6 $M_\odot$ model ($\sum^{13}$ C$_{\rm eff}$ = 3.1 × 10^{-7} $M_\odot$). This fact has obvious consequences on the production of *s*-process elements. The main neutron source in LMS-AGBs is the ^{13}C(α,n)^{16}O reaction (Gallino et al. 1998; Straniero et al. 2006). In those stars, a marginal contribution comes from the partial activation of the ^{22}Ne(α,n)^{25}Mg
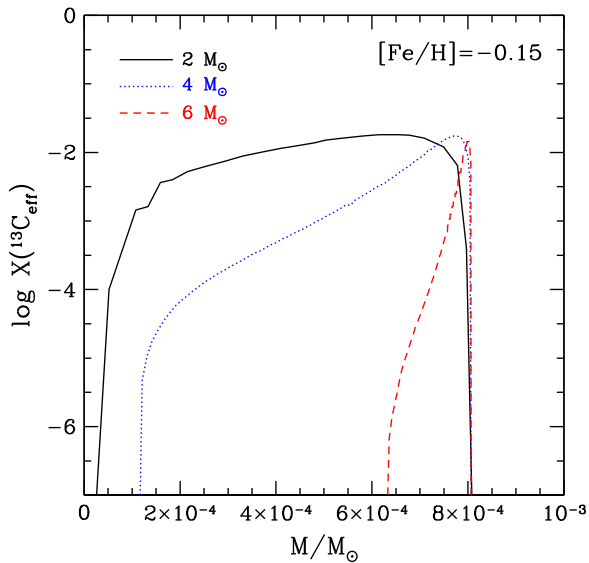
Figure 16. Mass extension of the *effective* ^{13}C in the pockets after the second TDU of the 2.0, 4.0, and 6.0 $M_\odot$ models with $Z = 10^{-2}$. See the text for details.

Figure 17. Final surface *s*-process enhancements: ls component (upper panel), hs component (middle panel), and lead (lower panel).

reaction. In Cristallo et al. (2011), we extensively described the final *s*-process surface distributions for AGB stars in this mass range. Their heavy element distributions show a progressive drift to heavier nuclei as the metallicity decreases. This is due to the fact that the neutron source (the ^{13}C$(\alpha,n)^{16}$O reaction) is of primary origin, while the seeds (^{56}Fe) scale with metallicity. Consequently, the lower the initial iron content, the larger the neutron-to-seed ratio. In IMS-AGBs stars, this scheme still holds, but with important differences. As already stressed in Straniero et al. (2014), these objects develop larger temperatures at the base of convective shells during TPs, thus efficiently activating the ^{22}Ne$(\alpha,n)^{25}$Mg reaction. Moreover, the contribution from the ^{13}C$(\alpha,n)^{16}$O reaction is lower due to thinner ^{13}C pockets, as shown previously. A clear sign of the ^{22}Ne$(\alpha,n)^{25}$Mg activation is reflected in the rubidium surface enhancement (see lower panel of Figure 12). It comes from the large production of ^{87}Rb, which is by-passed during radiative ^{13}C burning due to branchings at ^{85}Kr and, to a lesser extent, at ^{86}Rb (Straniero et al. 2014). Since the neutron exposure during the ^{22}Ne$(\alpha,n)^{25}$Mg episode is lower with respect to that of the ^{13}C$(\alpha,n)^{16}$O reaction, we also expect an overall reduction of *s*-process overabundances, in particular, for the second and third peaks of the *s*-process. This is confirmed by Figure 17 where we report the behavior of the three s-process peaks as a function of the metallicity. The corresponding data are tabulated in Tables 14–16. IMS-AGBs show definitely lower surface enhancements for the hs component (middle panel) and lead (lower panel). Note that this is also due to the reduced TDU efficiency characterizing those models (see Section 4). However, at low metallicities, the ls component (upper panel) of these models is comparable to that of less massive objects, thus demonstrating that the ^{22}Ne$(\alpha,n)^{25}$Mg reaction is efficiently at work. In a convective environment, neutrons cannot be released and piled up to synthesize the heaviest elements. This is particularly evident for lead, whose production is hampered in IMS-AGBs. The corresponding s-process indexes [hs/ls] and [Pb/hs] are reported in Figure 18. The corresponding data are tabulated in Tables 17 and 18. As
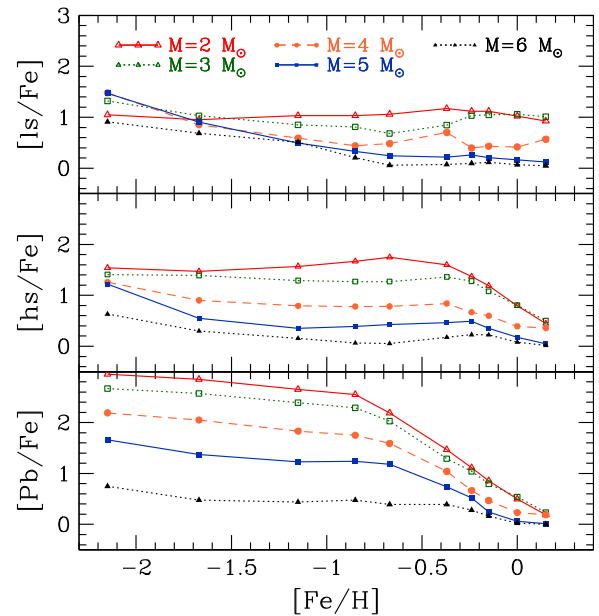
already anticipated in previous sections, we find a general reduction of the surface enhancements with respect to yields from Cristallo et al. (2011). However, the [hs/ls] and [Pb/hs] indexes remain almost unaltered because in LMS-AGBs models, those quantities are nearly independent of the evolutionary stage along the AGB, provided that the *s*-process enhancement is sufficiently large. As already stressed, this derives from the fact that the first ^{13}C pockets (the largest ones) are those governing the whole nucleosynthesis. Cristallo et al. (2015) recently computed the galactic chemical evolution of *s*-only isotopes and found that FRUITY models predict abundances which are too large for those nuclei. Thus, the reduction of LMS-AGBs yields we discussed in this paper may lead to better agreement with the observed solar *s*-only distribution. This problem will be addressed in a forthcoming paper.

The behavior of the [hs/ls] index strongly depends on the initial stellar mass. In fact, the efficient activation of the ^{22}Ne$(\alpha,n)^{25}$Mg reaction and the reduced contribution from the ^{13}C$(\alpha,n)^{16}$O reaction lead, in IMS-AGBs, to low [hs/ls] and [Pb/hs] indexes (see Figure 18). Another striking difference with respect to LMS-AGBs is that our massive AGBs do not reach an asymptotic value in the surface ratio between *s*-process peaks. This can be seen in Figure 19 where we plot [hs/ls] (upper panel) and [Pb/hs] (lower panel) as functions of the TDU number for selected masses with $Z = 2.3 \times 10^{-4}$. In LMS-AGBs, those quantities rapidly grow to an asymptotic value and then remain basically frozen (see the 2 $M_\odot$ curve). For larger masses, instead, both indexes reach a maximum and then start to decrease. This behavior is determined by the additional contribution from the ^{22}Ne$(\alpha,n)^{25}$Mg reaction, which is able to synthesize ls elements but not to produce hs ones. Unlike the ^{13}C pockets, the *imprint* of this neutron source progressively emerges with the TDU number. This is due to the fact that the largest temperatures are attained at the base of the convective shells generated by TPs toward the end of the AGB phase (see Figures 10 and 11). The larger the initial mass, the

Table 14
Final Surface [ls/Fe] (Representative of the First *s*-process Peak) for Different Initial Masses and Metallicities

Mass/[Fe/H]	−2.15	−1.67	−1.15	−0.85	−0.67	−0.37	−0.24	−0.15	0.00	0.15
1.3	9.82E−01	8.22E−01	4.80E−01	5.53E−01	4.26E−01	4.22E−01	1.22E−01	5.20E−02	0.00E+00	0.00E+00
1.5	1.17E+00	1.07E+00	7.06E−01	8.05E−01	7.27E−01	8.27E−01	6.95E−01	7.23E−01	6.27E−01	4.39E−01
2.0	1.05E+00	9.51E−01	1.03E+00	1.03E+00	1.06E+00	1.17E+00	1.12E+00	1.12E+00	1.02E+00	9.28E−01
2.5	1.23E+00	7.39E−01	9.15E−01	9.03E−01	1.02E+00	1.28E+00	1.31E+00	1.29E+00	1.19E+00	1.08E+00
3.0	1.32E+00	1.03E+00	8.53E−01	8.11E−01	6.79E−01	8.45E−01	1.03E+00	1.05E+00	1.06E+00	1.01E+00
4.0	1.48E+00	8.53E−01	5.88E−01	4.41E−01	4.82E−01	7.00E−01	3.96E−01	4.30E−01	4.16E−01	5.66E−01
5.0	1.47E+00	9.02E−01	4.95E−01	3.28E−01	2.43E−01	2.14E−01	2.58E−01	2.07E−01	1.62E−01	1.22E−01
6.0	9.10E−01	6.86E−01	5.09E−01	2.06E−01	5.80E−02	7.30E−02	9.60E−02	1.13E−01	6.90E−02	4.80E−02
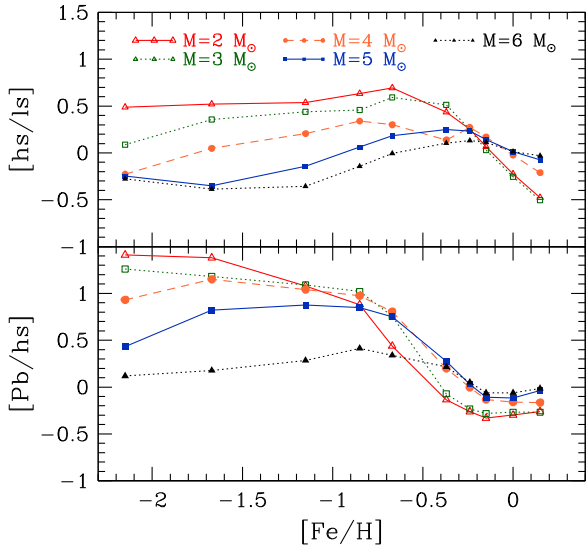
Figure 18. Final surface *s*-process indexes: [hs/ls] (upper panel) and [Pb/hs] (lower panel).

larger the TDU number needed to achieve such an asymptotic regime.[12] The [Pb/hs] does not depend on the activation of the ^{22}Ne$(\alpha,n)^{25}$Mg source, but only on the ^{13}C$(\alpha,n)^{16}$O one. Thus, the difference between LMS and IMS is less evident. Obviously, the larger the initial mass, the lower the [Pb/hs] value due to the decreasing contribution from the ^{13}C pockets.

7. DISCUSSION AND CONCLUSIONS

A detailed comparison between our LMS-AGB models and those from other groups have already been presented in Cristallo et al. (2011; see Section 5 of that paper). A similar analysis, but for IMS-AGBs, can be found in the study by Ventura et al. (2013), who compared their models with those published by Karakas (2010), as well as in Fishlock et al. (2014), who made a comparison with a subset of models presented by Straniero et al. (2014). Nevertheless, in Table 19, we report key quantities related to our 5 $M_\odot$ model with $Z = 1 \times 10^{-3}$ compared to similar available models in the literature (Ventura & D'Antona 2008; Fishlock et al. 2014). Note that there are other published papers on IMS-AGBs; however, they concentrate on different mass regimes (e.g., Siess 2007; Doherty et al. 2015) or present sets for a single metallicity (Herwig 2004). In general, this kind of comparison is not straightforward, since evolutionary codes significantly

differ in the adopted input physics (the treatment of convection and convective borders; the mass-loss rate; the initial chemical distribution; the opacities; the equation of state; the nuclear network; etc.). For instance, a direct comparison between our models and those presented by Ventura & D'Antona (2008) is difficult because not only is the treatment of convective borders different, but the theoretical recipe to model convection is also not the same (we use the MLT formulation by Cox 1968, while Ventura & D'Antona 2008 adopt the Full Spectrum of Turbulence of Canuto & Mazzitelli 1991). Other differences are the adopted mass-loss rate (Ventura & D'Antona 2008 use a calibrated version of the Bloecker 1995 mass-loss formula) as well as the initial chemical distribution (Ventura & D'Antona 2008 adopt the solar mixture by Grevesse & Sauval 1998 with an α element enhancement of 0.4). From an inspection of Table 19, it turns out that our model shows an HBB shallower than the model by Ventura & D'Antona (2008). It should be noted that in the models by Ventura & D'Antona (2008), mixing and burning are coupled. As already stressed, we aim to verify the effects of such coupling in our models in a future work. Actually, due to the adopted input physics (MLT for convection and mass-loss rate calibrated on galactic AGB stars), our model should be more similar to that of Fishlock et al. (2014). However, in this case the differences are also notable. At odds with our model, the 5 $M_\odot$ model of Fishlock et al. (2014) experienced a stronger HBB (as testified by the large temperatures attained at the base of the convective envelope during interpulse periods). In our models, we test the effects of changing the efficiency of mixing (we vary the free parameter of the MLT or the β parameter governing the convective velocity profile at the base of the convective envelope), the mixing scheme (by assuming instantaneous mixing in the envelope), the treatment of opacities at the border of the convective envelope, the adopted mass-loss rate (we run a model without mass loss and let it to evolve to larger core masses), or the equation of state (EOS; we substitute our treatment[13] by adopting the OPAL EOS 2005 at high temperatures (Rogers et al. 1996) and checking different transition temperatures to the low temperature regime). Those tests lead to variations of the ^{12}C/^{13}C ratio, but none of them show a significant activation of HBB. Thus, we are not able to explain such a discrepancy in the thermal stratification of our models with respect to Fishlock et al. (2014). Perhaps we should search for the origin in the dated EOS used by Fishlock et al. (2014). As reported[14] in Doherty et al. (2015), the perfect gas equation is adopted for fully ionized regions, the Saha EOS

---

[12] Note that the 6 $M_\odot$ model experiences more than 80 TDUs, but its [hs/ls] and [Pb/hs] are practically constant after the 50th TDU.

[13] Prada Moroni & Straniero (2002) for $T > 10^6$ K and the Saha equation for lower temperatures (see Straniero 1988).

[14] We suppose Fishlock et al. (2014) use the stellar code matrix.

Table 15
Final Surface [hs/Fe] (Representative of the Second s-process Peak) for Different Initial Masses and Metallicities

Mass/[Fe/H]	−2.15	−1.67	−1.15	−0.85	−0.67	−0.37	−0.24	−0.15	0.00	0.15
1.3	1.19E+00	1.11E+00	1.00E+00	1.14E+00	9.62E−01	7.16E−01	1.65E−01	2.50E−02	0.00E+00	0.00E+00
1.5	1.44E+00	1.41E+00	1.29E+00	1.46E+00	1.41E+00	1.31E+00	9.71E−01	7.83E−01	4.54E−01	1.15E−01
2.0	1.54E+00	1.47E+00	1.57E+00	1.67E+00	1.75E+00	1.60E+00	1.37E+00	1.19E+00	7.94E−01	4.50E−01
2.5	1.56E+00	1.20E+00	1.43E+00	1.48E+00	1.66E+00	1.69E+00	1.50E+00	1.27E+00	8.87E−01	5.42E−01
3.0	1.41E+00	1.39E+00	1.29E+00	1.27E+00	1.27E+00	1.36E+00	1.28E+00	1.08E+00	8.07E−01	5.03E−01
4.0	1.26E+00	9.01E−01	7.94E−01	7.81E−01	7.84E−01	8.38E−01	6.68E−01	5.99E−01	3.92E−01	3.55E−01
5.0	1.22E+00	5.49E−01	3.51E−01	3.90E−01	4.26E−01	4.63E−01	4.92E−01	3.51E−01	1.76E−01	4.80E−02
6.0	6.32E−01	3.00E−01	1.53E−01	6.20E−02	5.30E−02	1.78E−01	2.27E−01	2.25E−01	8.20E−02	1.70E−02

Table 16
Final Surface [Pb/Fe] (Representative of the Third s-process Peak) for Different Initial Masses and Metallicities

Mass/[Fe/H]	−2.15	−1.67	−1.15	−0.85	−0.67	−0.37	−0.24	−0.15	0.00	0.15
1.3	2.70E+00	2.52E+00	2.21E+00	2.08E+00	1.49E+00	5.88E−01	3.90E−02	3.00E−03	0.00E+00	0.00E+00
1.5	2.88E+00	2.80E+00	2.46E+00	2.38E+00	1.93E+00	1.17E+00	6.42E−01	3.99E−01	1.52E−01	2.00E−02
2.0	2.95E+00	2.85E+00	2.65E+00	2.55E+00	2.19E+00	1.47E+00	1.11E+00	8.57E−01	4.96E−01	1.89E−01
2.5	2.91E+00	2.66E+00	2.53E+00	2.45E+00	2.13E+00	1.57E+00	1.26E+00	1.00E+00	6.21E−01	2.56E−01
3.0	2.67E+00	2.57E+00	2.39E+00	2.29E+00	2.03E+00	1.29E+00	1.04E+00	7.96E−01	5.39E−01	2.35E−01
4.0	2.19E+00	2.05E+00	1.83E+00	1.75E+00	1.59E+00	1.04E+00	6.63E−01	4.68E−01	2.31E−01	1.89E−01
5.0	1.66E+00	1.37E+00	1.23E+00	1.24E+00	1.18E+00	7.39E−01	5.22E−01	2.42E−01	6.10E−02	1.20E−02
6.0	7.51E−01	4.78E−01	4.37E−01	4.75E−01	3.92E−01	3.94E−01	2.78E−01	1.63E−01	2.20E−02	3.00E−03

in partially ionized regions (following the method of Bærentzen 1965), while EOS from Beaudet & Tassoul (1971) is used for relativistic or electron-degenerate gas. However, a discussion of the proper EOS to be used in AGB stellar models, as well on the effects induced by adopting a different EOS, is beyond the goals of this paper.

More meaningful conclusions can be derived by comparing theoretical models to observed quantities. As discussed in Section 4, the majority of our models present final C/O ratios larger than 1. Their observational counterparts are C-rich stars, whose luminosity function, which links a physical quantity (the luminosity) with the chemistry (its surface carbon abundance), represents a good test indicator for theoretical prescriptions. A revision of the observational galactic luminosity function of carbon stars (LFCS) was recently presented by Guandalini & Cristallo (2013). Such an LFCS is plotted in Figure 20 (dotted histogram), together with the theoretical LFCS obtained with models by Cristallo et al. (2011; dashed histogram) and with models presented in this paper (continuous histogram). With respect to our previous estimate, we note a marginal shift to low luminosities as a consequence of the reduced TP-AGB lifetimes caused by the erroneous treatment in the opacities of the most external layers of the star. In the upper right corner of Figure 20, we report the LFCS derived by considering the contribution of IMS-AGBs only. Those objects populate the high-luminosity tail of the LFCS. However, their contribution to the whole distribution is practically negligible. Thus, at variance with LMS-AGBs, the LFCS cannot be fruitfully used to constrain the physical evolution of IMS-AGBs.

Another interesting quantity that can be used to constrain theoretical models is the initial-to-final mass relation. This relation depends on the core mass of the H-exhausted core attained at the end of the TP-AGB phase. As already noted in Section 4, for the more massive models presented here, the presence of the SDU induces important variations in the mass of the H-exhausted core. In Figure 21, we compare a selection of our models to the semi-empirical initial-to-final mass

relation of Weidemann (2000) as well as to the observational data of Open Clusters (Ferrario et al. 2005; Catalán et al. 2008; Dobbie et al. 2009; Williams et al. 2009; Zhao et al. 2012; Kalirai et al. 2014). In Table 20, we report the final core masses of the whole FRUITY set. Our theoretical models agree well with the semi-empirical initial-to-final mass relation of Weidemann (2000), however, showing larger core masses for low-mass objects. When looking at observations, the situation becomes more complex. For a fixed initial mass, observations present a rather wide spread up to ∼0.5 $M_\odot$. Thus, firm conclusions cannot be drawn. Moreover, it must be taken into account that many observations are indirectly affected by the uncertainty characterizing stellar models. In fact, while the WD mass can be determined based on spectroscopic data, the initial mass is generally derived by estimating the cluster age. This evaluation is done by means of theoretical relations among the mass, age, and turn-off luminosity. Thus, the result depends on the physical recipe adopted to compute the cluster isocrone. In Figure 21, we report core masses at the last computed model (i.e., when TDU ceases to operate). Computing the following evolutionary phases is made difficult by the treatment of the most external layers. The final surface chemistry remains frozen up to the WD phase unless a very Late TP occurs (Iben et al. 1983; Herwig et al. 2011). Note that only under the hypothesis of a strong final super-wind episode, capable of instantaneously removing the whole remaining envelope, core masses at the last TDU would coincide with WD masses. Alternatively, the star experiences additional TPs without TDU up to the almost complete erosion of the convective envelope. Then, we also performed an extrapolation of the core mass. For models with an initial mass larger than 3 $M_\odot$, the differences in the core mass between the last computed model and the extrapolated number are neglibile (lower than 0.01 $M_\odot$), while in the LMS regime they become appreciable (up to 0.035 $M_\odot$). The extrapolated final masses are reported in the ph-FRUITY database.

Table 17
s-process Index [hs/ls] for Different Initial Masses and Metallicities

Mass/[Fe/H]	−2.15	−1.67	−1.15	−0.85	−0.67	−0.37	−0.24	−0.15	0.00	0.15
1.3	2.10E−01	2.92E−01	5.20E−01	5.81E−01	5.37E−01	2.94E−01	4.30E−02	−2.70E−02	0.00E+00	0.00E+00
1.5	2.78E−01	3.40E−01	5.84E−01	6.50E−01	6.83E−01	4.84E−01	2.76E−01	6.00E−02	−1.73E−01	−3.24E−01
2.0	4.87E−01	5.21E−01	5.38E−01	6.34E−01	6.95E−01	4.37E−01	2.53E−01	6.60E−02	−2.25E−01	−4.78E−01
2.5	3.33E−01	4.56E−01	5.12E−01	5.74E−01	6.37E−01	4.10E−01	1.89E−01	−2.00E−02	−3.01E−01	−5.38E−01
3.0	8.80E−02	3.57E−01	4.40E−01	4.59E−01	5.92E−01	5.12E−01	2.50E−01	3.00E−02	−2.55E−01	−5.04E−01
4.0	−2.27E−01	4.80E−02	2.06E−01	3.40E−01	3.01E−01	1.38E−01	2.72E−01	1.70E−01	−2.40E−02	−2.11E−01
5.0	−2.48E−01	−3.52E−01	−1.44E−01	6.20E−02	1.83E−01	2.49E−01	2.34E−01	1.44E−01	1.30E−02	−7.40E−02
6.0	−2.78E−01	−3.86E−01	−3.56E−01	−1.44E−01	−5.00E−03	1.05E−01	1.31E−01	1.12E−01	1.30E−02	−3.00E−02

Table 18
s-process Index [Pb/hs] for Different Initial Masses and Metallicities

Mass/[Fe/H]	−2.15	−1.67	−1.15	−0.85	−0.67	−0.37	−0.24	−0.15	0.00	0.15
1.3	1.51E+00	1.40E+00	1.21E+00	9.40E−01	5.26E−01	−1.28E−01	−1.26E−01	−2.20E−02	0.00E+00	0.00E+00
1.5	1.44E+00	1.39E+00	1.17E+00	9.27E−01	5.19E−01	−1.45E−01	−3.30E−01	−3.84E−01	−3.02E−01	−9.50E−02
2.0	1.41E+00	1.38E+00	1.08E+00	8.79E−01	4.38E−01	−1.35E−01	−2.62E−01	−3.31E−01	−2.98E−01	−2.61E−01
2.5	1.34E+00	1.47E+00	1.10E+00	9.75E−01	4.72E−01	−1.21E−01	−2.31E−01	−2.68E−01	−2.66E−01	−2.86E−01
3.0	1.26E+00	1.18E+00	1.09E+00	1.02E+00	7.56E−01	−7.10E−02	−2.33E−01	−2.82E−01	−2.68E−01	−2.68E−01
4.0	9.31E−01	1.15E+00	1.04E+00	9.74E−01	8.04E−01	1.98E−01	−5.00E−03	−1.32E−01	−1.60E−01	−1.66E−01
5.0	4.32E−01	8.22E−01	8.76E−01	8.48E−01	7.50E−01	2.76E−01	3.00E−02	−1.09E−01	−1.15E−01	−3.60E−02
6.0	1.19E−01	1.78E−01	2.84E−01	4.13E−01	3.39E−01	2.16E−01	5.10E−02	−6.20E−02	−6.00E−02	−1.50E−02

Table 19
Physical and Chemical Properties of our 5 $M_\odot$ Model with $Z = 10^{-3}$
Compared to Fishlock et al. 2014 (FI14) and Ventura &
D'Antona 2008 (VD08)

|	This paper	FI14	VD08
M_H^{INI} ($M_\odot$)	0.92	0.92	0.91
M_H^{END} ($M_\odot$)	0.94	0.95	0.94
TP	25	94	53
λ_{max}	0.69	0.95	0.50
T_{CE}^{max} (K)	3.0×10^7	9.2×10^7	1.0×10^8
Y	0.33	0.36	0.32
[C/Fe]	1.16	0.36	0.13
[N/Fe]	0.59	2.45	1.70
[O/Fe]	−0.05	−0.20	−0.06
[F/Fe]	−0.05	0.36	−1.16
[Na/Fe]	0.51	0.87	0.60
[Mg/Fe]	0.07	0.61	0.35
[Al/Fe]	0.04	0.74	1.02
[ls/Fe]	0.50	1.33	⋯
[hs/Fe]	0.35	0.51	⋯
[Pb/Fe]	1.23	0.25	⋯

Spectroscopic observations capable of constraining the evolution of IMS-AGBs are rare. The lack of C-stars in MCs with luminosities larger than $M_{bol} = -6$ led Wood et al. (1983) to the conclusion that CNO cycling is at work in upper AGB stars, preventing them from becoming C-rich. Actually, it cannot be excluded that C-rich stars with high luminosities exist, since they could be embedded in an opaque dust-rich cloud masking them from observations. For instance, van Loon et al. (1999) found giant C-rich stars up to $M_{bol} = -6.7$, thus demonstrating that in those objects TDU is at work and that HBB is not efficient enough to make those stars O-rich. More recently, a restricted sample of galactic O-rich giant stars has been presented by García-Hernández et al. (2006). Unfortunately, in the spectral regions under analysis, the adopted synthetic spectra do not have the necessary resolution to precisely fix the carbon, nitrogen, and oxygen abundances (as well as the $^{12}C/^{13}C$ ratio, see García-Hernández et al. 2007). Moreover, for galactic stars, the determination of the absolute magnitude is highly uncertain due to the difficulties in determining the distance of those objects. Thus, apart from the derived C/O ratio (less than 0.75) and the lithium abundance, they cannot be used to constrain HBB. However, our models can be tested by checking their s-process element abundances. Stars observed by García-Hernández et al. (2006) have been found to be extremely rubidium-rich and zirconium poor. This is at odds with theoretical s-process expectations. However, more recently, the same authors (Zamora et al. 2014)
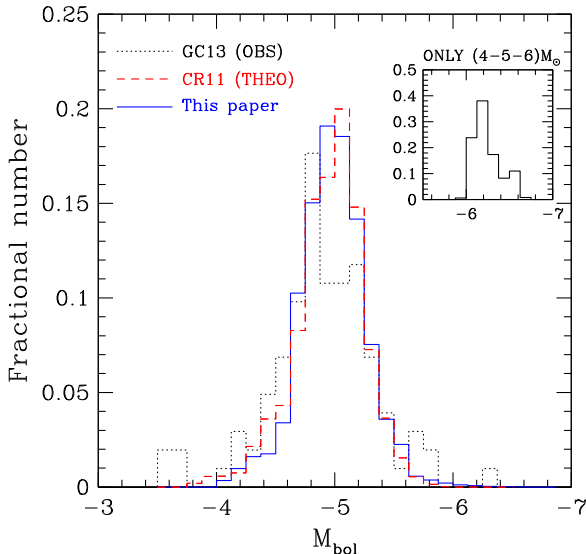
re-analyzed four stars demonstrating that the inclusion of a circumstellar component leads to definitely lower Rb surface abundances without appreciably modifying Zr data. Looking to their Table 1, we note that for the galactic sample, all stars are compatible within errors with null s-process enrichments (for both Rb and Zr), except for IRAS 18429-1721, which shows an appreciable Rb enrichment ([Rb/M] = 1.0 ± 0.4). A more useful comparison could be made with a similar sample, but for stars belonging to MCs (García-Hernández et al. 2009). In that case, distances are better known and bolometric magnitudes can be derived. On average, stars are Zr-poor (some of them showing some enhancement), and thus agree with our models. Those objects are Rb-rich. However, as for the galactic sample, a decrease in the Rb abundance is expected when considering a circumstellar component, as demonstrated by the LMC star (IRAS 04498-6842; Zamora et al. 2014). The rubidium surface enrichment of this star ([Rb/M] = 1.5 ± 0.7) is not in agreement with our models, even when taking into account the large observational errors. Its bolometric magnitude (M_{bol} = −7.72) may indicate a larger stellar mass with respect to those presented in this paper. At the same time, however, it could be proof of the activation of HBB, which implies larger surface luminosities with respect to those expected from the core-luminosity relation (see, e.g., Bloecker & Schoenberner 1991). In conclusion, apart from a single object, our models do not disagree with the discussed observational data. Another interesting sample is that by McSaveney et al. (2007), who presented C, N, and O abundances in two O-rich luminous giants belonging to the LMC (NGC 1866#4 and HV2576). In particular, those authors found strong carbon depletion (∼1 dex) coupled with clear nitrogen enhancement (∼1 dex). They concluded that this is proof of ongoing HBB in the analyzed stars. However, alternative theories could be explored. First, we note that before entering the TP-AGB phase, FDU and SDU increase the surface N abundance by a factor of three. This is not sufficient to reproduce observations. However, it should be stressed that additional physical phenomena may produce similar abundance patterns. An illuminating case is represented by rotation. Models presented in this paper do not take into account the effects of rotation. In Piersanti et al. (2013), we demonstrated that mixing induced by rotation may significantly change the final surface theoretical distributions of LMS-AGB models. Rotation may also induce non-canonical mixing in larger masses. In particular, during the MS phase, meridional circulations (von Zeipel 1924a, 1924b) may work in the layers between the inner border of the convective envelope and the upper border of the receding H-burning convective core. In that case, mixing would develop in a region that previously experienced CN cycling. Later, after the occurrence of FDU, the surface CN abundances could vary.

Table 20
The H-exhausted Core Mass at the End of the AGB Phase (in Solar Units)

Mass/[Fe/H]	−2.15	−1.67	−1.15	−0.85	−0.67	−0.37	−0.24	−0.15	0.00	0.15
1.3	0.658	0.631	0.628	0.625	0.624	0.605	0.610	0.604	0.601	0.596
1.5	0.667	0.645	0.635	0.628	0.623	0.612	0.623	0.600	0.604	0.613
2.0	0.676	0.671	0.656	0.636	0.631	0.621	0.623	0.617	0.617	0.612
2.5	0.749	0.724	0.699	0.674	0.654	0.629	0.628	0.621	0.624	0.619
3.0	0.815	0.810	0.789	0.760	0.743	0.689	0.668	0.652	0.652	0.634
4.0	0.876	0.874	0.867	0.861	0.854	0.828	0.826	0.813	0.800	0.747
5.0	0.949	0.946	0.936	0.926	0.920	0.887	0.873	0.872	0.864	0.842
6.0	1.060	1.050	1.040	1.020	1.010	0.974	0.950	0.927	0.935	0.908
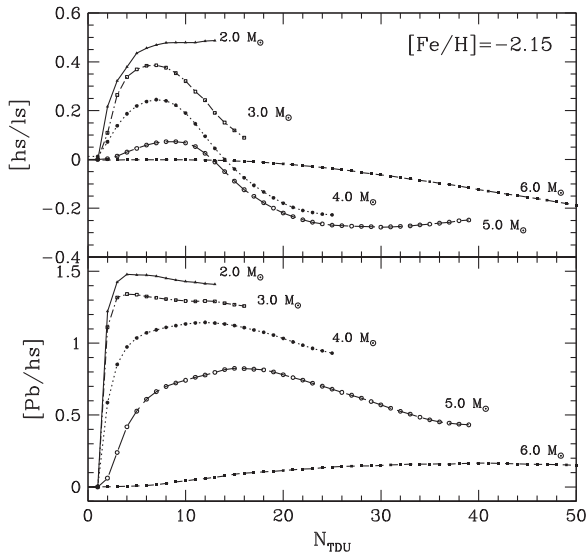
Figure 19. [hs/ls] (upper panel) and [Pb/hs] (lower panel) as a function of the TDU numbers for selected models with [Fe/H] = −2.15.

Figure 21. FRUITY models Initial-to-final mass relations for selected metallicities, compared to the semi-empirical relation from Weidemann (2000) and to Open Clusters observations.

Figure 20. Our new theoretical LFCS (solid curve) compared to our previous estimate (dashed curve; CR11: Cristallo et al. 2011) and observations (dashed curve; GC13: Guandalini & Cristallo 2013).

We test the effects of rotation on a $6\,M_\odot$ model with $Z = 10^{-2}$ and different initial rotation velocities. We find that models rotating on the zero-age main sequence (ZAMS) with $v_{rot}^{ini} \sim 100\,{\rm km\,s^{-1}}$ (thus not as high for stars with this mass)

already show a large C depletion (−1 dex) and a strong nitrogen enhancement (+0.7 dex). Note that similar conclusions have already been derived by Georgy et al. (2013), even with a different formulation for the transport of angular momentum.

Other useful constraints to theoretical models come from the study of abundances derived in planetary nebulae (PNs), which lie between the tip of the AGB and the WD cooling sequence (for a review see Balick & Frank 2002). During that evolutionary phase, the strong mass loss practically peels the H-exhausted core. The star evolves toward higher surface temperatures at almost constant luminosity and, when the ionization of the lost gas begins, a PN emerges. It has been shown (see García-Hernández & Górny 2014 for an updated study) that a consistent fraction of PNs are N-rich (the so-called type I PNs). The most ^{14}N-enriched PNs are not accessible by our models. However, a considerable fraction of the sample can be reproduced by taking into account the variations in CNO abundances caused by the occurrence of FDU and/or SDU. Moreover, the effects induced by rotation (see above) or the presence of a companion (De Marco 2009) could complicate the physical and chemical behavior of PNs. Finally, we stress that a precise determination of the PN masses is not an easy task (as always for galactic objects). It could be that the most N-rich PNs are remnants of the evolution of massive AGBs

(7–8–9 $M_\odot$; the so-called super-AGBs), whose evolution is not explored in this paper.

Finally, let us stress that, to date, no signature of HBB has been found in pre-solar grains. In 2007, it was claimed that the composition of the peculiar spinel grain OC2 could be attributed to the nucleosynthesis induced by HBB in a massive AGB star (Lugaro et al. 2007). However, in order to reconcile theoretical models and laboratory measurements, a modification of nuclear cross sections was needed. Later, the same authors (Iliadis et al. 2008) rejected such a hypothesis, identifying a low-mass star experiencing additional non-convective mixing as the best candidate to explain the isotopic signatures of that grain (see also Palmerini et al. 2013). This does not necessarily imply that pre-solar SiC grains carrying the signature of HBB do not exist, but rather that they have not been discovered yet.

REFERENCES

Abia, C., Cunha, K., Cristallo, S., et al. 2010, ApJL, 715, L94
Abia, C., Cunha, K., Cristallo, S., et al. 2011, ApJL, 737, L8
Abia, C., Recio-Blanco, A., de Laverny, P., et al. 2009, ApJ, 694, 971
Bærentzen, J. 1965, ZAp, 62, 221
Balick, B., & Frank, A. 2002, ARA&A, 40, 439
Beaudet, G., & Tassoul, M. 1971, A&A, 13, 209
Bloecker, T. 1995, A&A, 297, 727
Bloecker, T., & Schoenberner, D. 1991, A&A, 244, L43
Böhm-Vitense, E. 1958, ZAp, 46, 108
Canuto, V. M., & Mazzitelli, I. 1991, ApJ, 370, 295
Catalán, S., Isern, J., García-Berro, E., et al. 2008, A&A, 477, 213
Cox, J. P. 1968, Principles of Stellar Structure: Physical Principles, Vol. 1
    (New York: Gordon and Breach)
Cristallo, S., Abia, C., Straniero, O., & Piersanti, L. 2015, ApJ, 801, 53
Cristallo, S., Di Leva, A., Imbriani, G., et al. 2014, A&A, 570, A46
Cristallo, S., Piersanti, L., Straniero, O., et al. 2011, ApJS, 197, 17
Cristallo, S., Straniero, O., Gallino, R., et al. 2009, ApJ, 696, 797
Cristallo, S., Straniero, O., Lederer, M. T., & Aringer, B. 2007, ApJ, 667, 489
De Marco, O. 2009, PASP, 121, 316
Dobbie, P. D., Napiwotzki, R., Burleigh, M. R., et al. 2009, MNRAS,
    395, 2248
Doherty, C. L., Gil-Pons, P., Siess, L., Lattanzio, J. C., & Lau, H. H. B. 2015,
    MNRAS, 446, 2599
Dominguez, I., Chieffi, A., Limongi, M., & Straniero, O. 1999, ApJ, 524, 226
Ferrario, L., Wickramasinghe, D., Liebert, J., & Williams, K. A. 2005,
    MNRAS, 361, 1131
Fishlock, C. K., Karakas, A. I., Lugaro, M., & Yong, D. 2014, ApJ, 797, 44
Gallino, R., Arlandini, C., Busso, M., et al. 1998, ApJ, 497, 388
García-Hernández, D. A., García-Lario, P., Plez, B., et al. 2006, Sci, 314, 1751
García-Hernández, D. A., García-Lario, P., Plez, B., et al. 2007, A&A,
    462, 711
García-Hernández, D. A., & Górny, S. K. 2014, A&A, 567, A12
García-Hernández, D. A., Manchado, A., Lambert, D. L., et al. 2009, ApJL,
    705, L31
Georgy, C., Ekström, S., Granada, A., et al. 2013, A&A, 553, A24
Goriely, S., & Siess, L. 2004, A&A, 421, L25
Gratton, R. G., Sneden, C., Carretta, E., & Bragaglia, A. 2000, A&A, 354, 169
Grevesse, N., & Sauval, A. J. 1998, SSRv, 85, 161
Guandalini, R., & Cristallo, S. 2013, A&A, 555, A120
Herwig, F. 2004, ApJS, 155, 651
Herwig, F. 2005, ARA&A, 43, 435
Herwig, F., Pignatari, M., Woodward, P. R., et al. 2011, ApJ, 727, 89
Iben, I., Jr. 1973, ApJ, 185, 209
Iben, I., Jr., Kaler, J. B., Truran, J. W., & Renzini, A. 1983, ApJ, 264, 605
Iben, I., Jr., & Renzini, A. 1983, ARA&A, 21, 271
Iliadis, C., Angulo, C., Descouvemont, P., Lugaro, M., & Mohr, P. 2008,
    PhRvC, 77, 045802
Kalirai, J. S., Marigo, P., & Tremblay, P.-E. 2014, ApJ, 782, 17
Karakas, A. I. 2010, MNRAS, 403, 1413
Karakas, A. I., & Lattanzio, J. C. 2014, PASA, 31, 30
Lebzelter, T., Straniero, O., Hinkle, K. H., Nowotny, W., & Aringer, B. 2015,
    A&A, 578, A33
Lederer, M. T., & Aringer, B. 2009, A&A, 494, 403
Liu, N., Savina, M. R., Davis, A. M., et al. 2014, ApJ, 786, 66
Liu, N., Savina, M. R., Gallino, R., et al. 2015, ApJ, 803, 12
Lodders, K. 2003, ApJ, 591, 1220
Lugaro, M., Karakas, A. I., Nittler, L. R., et al. 2007, A&A, 461, 657
Marigo, P. 2002, A&A, 387, 507
Marigo, P., & Aringer, B. 2009, A&A, 508, 1539
McSaveney, J. A., Wood, P. R., Scholz, M., Lattanzio, J. C., & Hinkle, K. H.
    2007, MNRAS, 378, 1089
Nittler, L. R., Alexander, C. M. O., Gao, X., Walker, R. M., & Zinner, E. 1997,
    NuPhA, 621, 113
Nucci, M. C., & Busso, M. 2014, ApJ, 787, 141
Palmerini, S., La Cognata, M., Cristallo, S., & Busso, M. 2011, ApJ, 729, 3
Palmerini, S., Sergi, M. L., La Cognata, M., et al. 2013, ApJ, 764, 128
Piersanti, L., Cristallo, S., & Straniero, O. 2013, ApJ, 774, 98
Prada Moroni, P. G., & Straniero, O. 2002, ApJ, 581, 585
Prada Moroni, P. G., & Straniero, O. 2009, A&A, 507, 1575
Rogers, F. J., Swenson, F. J., & Iglesias, C. A. 1996, ApJ, 456, 902
Siess, L. 2007, A&A, 476, 893
Sparks, W. M., & Endal, A. S. 1980, ApJ, 237, 130
Straniero, O. 1988, A&AS, 76, 157
Straniero, O., Cristallo, S., & Piersanti, L. 2014, ApJ, 785, 77
Straniero, O., Domínguez, I., Cristallo, S., & Gallino, R. 2003a, PASA, 20, 389
Straniero, O., Domínguez, I., Imbriani, G., & Piersanti, L. 2003b, ApJ,
    583, 878
Straniero, O., Gallino, R., & Cristallo, S. 2006, NuPhA, 777, 311
Sugimoto, D. 1971, PThPh, 45, 761
Sweigart, A. V., Greggio, L., & Renzini, A. 1990, ApJ, 364, 527
Uttenthaler, S. 2013, A&A, 556, A38
van Loon, J. T., Cioni, M.-R. L., Zijlstra, A. A., & Loup, C. 2005, A&A,
    438, 273
van Loon, J. T., Groenewegen, M. A. T., de Koter, A., et al. 1999, A&A,
    351, 559
Vassiliadis, E., & Wood, P. R. 1993, ApJ, 413, 641
Ventura, P., & D'Antona, F. 2005a, A&A, 431, 279
Ventura, P., & D'Antona, F. 2005b, A&A, 439, 1075
Ventura, P., & D'Antona, F. 2006, A&A, 457, 995
Ventura, P., & D'Antona, F. 2008, A&A, 479, 805
Ventura, P., Di Criscienzo, M., Carini, R., & D'Antona, F. 2013, MNRAS,
    431, 3642
Ventura, P., & Marigo, P. 2010, MNRAS, 408, 2476
von Zeipel, H. 1924a, MNRAS, 84, 665
von Zeipel, H. 1924b, MNRAS, 84, 684
Weidemann, V. 2000, A&A, 363, 647
Whitelock, P. A., Feast, M. W., van Loon, J. T., & Zijlstra, A. A. 2003,
    MNRAS, 342, 86
Williams, K. A., Bolte, M., & Koester, D. 2009, ApJ, 693, 355
Wood, P. R. 2007, in ASP Conf. Ser. 374, From Stars to Galaxies Building the
    Pieces to Build Up the Universe, ed. A. Vallenari et al. (San Francisco, CA:
    ASP), 47
Wood, P. R., Bessell, M. S., & Fox, M. W. 1983, ApJ, 272, 99
Zamora, O., García-Hernández, D. A., Plez, B., & Manchado, A. 2014, A&A,
    564, L4
Zhao, J. K., Oswalt, T. D., Willson, L. A., Wang, Q., & Zhao, G. 2012, ApJ,
    746, 144